scientific reports

Check for updates

OPEN

The electronic structure of 1/1 ZnMgHf and its consequences for the electronic transport of the quasicrystal

Ireneusz Buganski[1]✉, Stanislav Vrtnik[2,3], Radoslaw Strzalka[1], Jože Luzar[2], Janusz Wolny[1] & Nobuhisa Fujita[4]

This paper presents a detailed density functional theory study of the 1/1 periodic approximant Zn-Mg-Hf crystal structure, which is a close analog of the F-type Bergman-type quasicrystal. Two structural models, Bergman-like and Tsai-like, are examined to investigate their energetic stability, electronic structure, and transport properties. The Tsai-like model, characterized by additional multicenter bonds, higher Madelung stability and significant charge transfer, is found to be energetically more favorable by 10.9 meV per unit cell. Fermi surface nesting features may be related to quasicrystal stabilization mechanisms. Study utilizes Electron Localization Function, non-covalent bond analysis and Maximally Localized Wannier Functions. Experimental resistivity and magnetoresistance measurements confirm metallic behavior with nontrivial scattering mechanisms and subquadratic magnetoresistance. This study emphasizes the combined role of electronic sp-d hybridization, charge transfer, and multicenter bonds in the stabilization of Zn-based periodic approximant crystals. The present findings can be extended to the quasicrystalline phase.

The Zn-Mg-(Hf, Zr, Ti) family of 1/1 periodic approximant crystals to the face-centered (F) type Bergman-type quasicrystal is unique. The number of cubic approximants, i.e., 1/1, 2/1 or even 3/2, on the basis of the notation of Elser & Henley[1], is sparse in the Bergman-type family but rich in the Tsai- and Mackay-type families. In particular, the model of 3/2 $Al_{69.1}Pd_{22}Cr_{2.1}Fe_{6.8}$[2] laid the foundation for the model of the F-type Mackay quasicrystal[3]. The fact that the F phase is right next to the primitive (P) phase is also exceptional[4,5]. The composition of the stable F-type ZnMgHf quasicrystal is $Zn_{80.7}Mg_{11.7}Hf_{7.5}$[6], whereas the P phase contains approximately 85% Zn[7].

The cohabitation of Bergman-type local motives in Tsai-type quasicrystals is evident on the basis of the model of icosahedral $Cd_{5.7}Yb$ by Takakura et al.[8]. In addition, Li et al.[9] reported that a 2/1 periodic approximant crystal of the Tsai type is describable with a pseudo-Bergman cluster. The same applies to 1/1 approximants[10]. Furthermore, the structure of icosahedral $Cd_{5.7}Yb$ can be viewed as being built of Bergman clusters[11].

The atomic model for 1/1 periodic approximant crystals was obtained in 2008[12]. The phase crystallizes in $Pm\bar{3}$ with a 13.6740 (11) Å lattice constant. The list of atomic positions for Zn-Mg-Hf is given in Table 1, and the visualization is shown in Fig. 1. Importantly, Zn14 (atom 'b' in[10] forms an octahedral shell between the icosahedron and soccerball polyhedron. The inner shell of the body-centered rhombic triacontahedral cluster (B-RTH) is highly disordered and interpreted as a freely rotating dodecahedron[12]. This contrasts with the inner icosahedron found in the vertex-centered rhombic triacontahedral cluster (V-RTH). Atom 'b' (Zn14) is partially occupied together with two neighboring sites (Zn15). Zn14 would be fully occupied in the Tsai-type structure and empty in the Bergman-type structure. If present in the Bergman structure, it should be electropositive[13].

In this work, we perform Density Functional Theory (DFT) electronic structure calculations to reveal the origin of structural stabilization and the reasons why the structure is on the verge between being ideal Bergman-

[1]Faculty of Physics and Applied Computer Science, AGH University of Krakow, Krakow, Poland. [2]Jožef Stefan Institute, Jamova 39, Ljubljana SI-1000, Slovenia. [3]Faculty of Mathematics and Physics, University of Ljubljana, Jadranska 19, Ljubljana SI- 1000, Slovenia. [4]Institute of Multidisciplinary Research for Advanced Materials, Tohoku University, Sendai 980-8577, Japan. ✉email: Ireneusz.Buganski@fis.agh.edu.pl

Atom label	Wyckoff Site	SOF	x	y	z
Hf1	6 g	1	0.30315	0.5	0
Mg2	12j	1	0.3086	0.1170	0
Mg4/Hf4	8i	0.898/0.102	0.18855	0.18855	0.18855
Zn1	12j	1	0.09602	0.15563	0
Zn3	24 L	1	0.19090	0.40626	0.16214
Zn5	6 g	1	0.09277	0.5	0
Zn6	24 L	1	0.35283	0.31587	0.09906
Zn7	12k	1	0.2314	0.5	0.3433
Zn8/Mg8	12k	0.967/0.033	0.3686	0.5	0.2008
Zn10/Mg10	6f	0.833/0.167	0	0.5	0.20424
Zn13	12j	1	0.18553	0.31576	0
Zn14	6 h	0.5	0.5	0.5	0.1086
Zn15	12k	0.5	0.5	0.4089	0.031
Zn12/Mg12	8i	0.412/0.588	0.3118	0.3118	0.3118
Zn17	24 L	0.077	0.4050	0.3867	0.4248
Zn18	12k	0.368	0.3514	0.5	0.5439
Zn19	12k	0.108	0.5	0.3671	0.436

Table 1. The list of atoms in the Zn-Mg-Hf model by Gómez et al.[12]. The site occupancy factor (SOF) is given for all the sites.

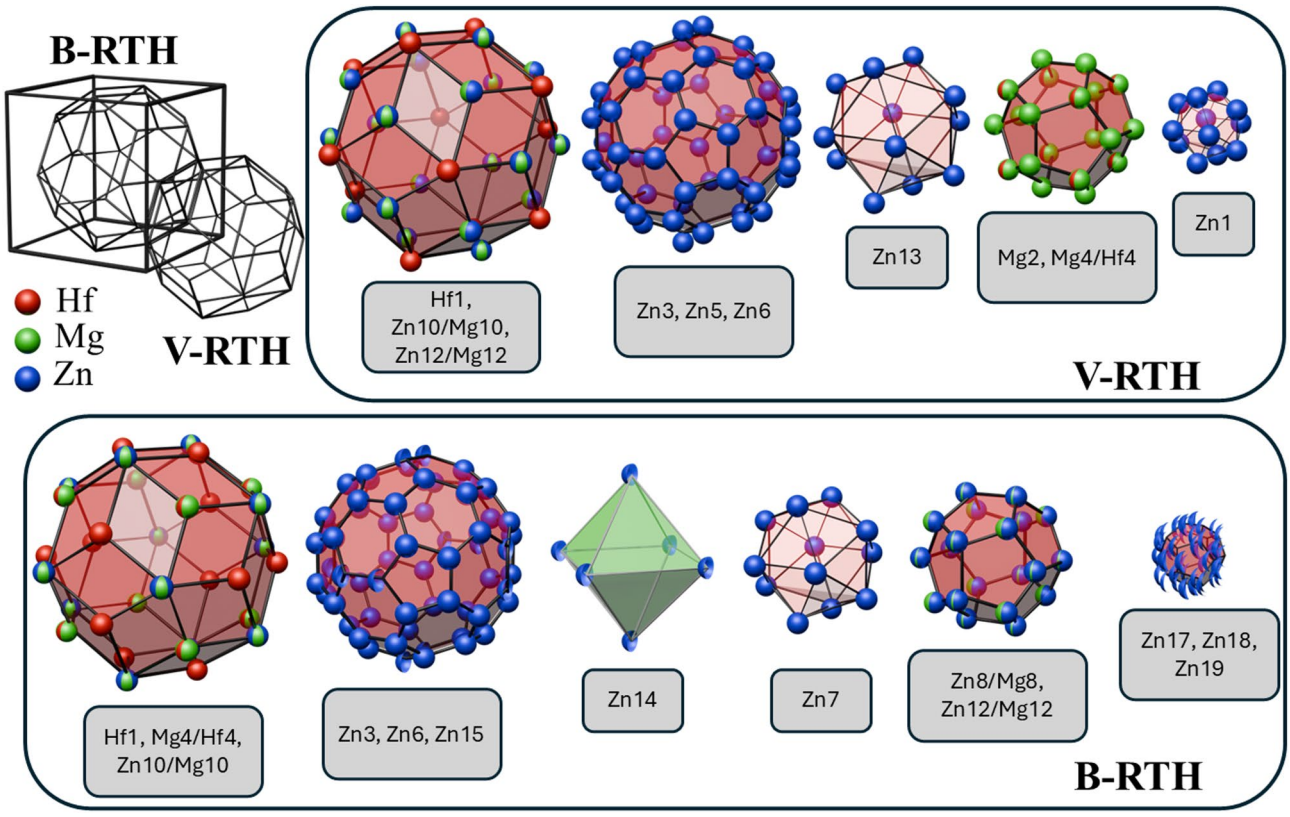

Fig. 1. Visualization of the atomic structure of Zn-Mg-Hf was performed as described by Gómez et al.[12]. In the B-RTH cluster, an additional shell, an octahedron, is created by Zn14 atoms with 0.5 SOF. Zn14 is in direct proximity to Zn15, which is a partially occupied site of the soccerball shell.

type and Tsai-type. Calculations are performed for Zn-Mg-Hf (the refined composition is $Zn_{79.8}Mg_{15.9}Hf_{4.3}$) only because the structure has the lowest R factor among those solved by Gómez et al.[12].

Computational details

The DFT calculations were performed with the use of the QUANTUM ESPRESSO v.6.7 suite[14–16] with multicore processing via the PLGrid infrastructure. The computations utilized projector-augmented wave-based pseudopotentials with core correction and a scalar-relativistic approximation[17]. The kinetic energy cutoff for the charge density was set at 400 Ry, and for wavefunctions, it was set at 60 Ry. The electronic exchange-correlation potential was treated with the Perdew–Burke–Ernzerhof generalized gradient approximation (GGA)[18]. The valance configuration for each element is: Zn – $4s^2\ 4p^{0.3}\ 3d^{9.70}$, Mg – $2s^2\ 3s^2\ 2p^6$ and Hf – $5s^2\ 6s^2\ 5p^6\ 5d^2$.

Two models are considered. Both have all the sites fully occupied. The Zn8/Mg8 site is fully occupied by Zn. The same applies to Zn10/Mg10. The Zn12/Mg12 and Mg4/Hf4 sites are fully occupied by Mg. The partially occupied sites in the center of the B-RTH cluster are positioned in the vertices of the dodecahedron. The first model, called onward B1, has the Zn14 atom removed and the Zn15 site fully occupied. The second model, called T1, has the fully occupied Zn14 site. This requires the removal of some of the Zn15 atoms. Zn15 lies close to faces with periodic boundary conditions; therefore, it is sufficient to remove two atoms close to 3 of the 6 faces. The total number of atoms in the unit cell for both models is 174 (Zn-140, Mg-28, Hf-6), with 2032 electrons.

Both models are initially relaxed on a $4 \times 4 \times 4$ k-point grid based on the Monkhorst-Pack approach[19] with the Methfessel-Paxton smearing parameter set to 0.02[20,21]. The total force threshold during ionic minimization is 0.001. We used variable-cell relaxation with a constraint set on the Bravais lattice.

After relaxation, self-consistent field (SCF) calculations were performed on a $5 \times 5 \times 5$ grid with the Methfessel-Paxton smearing parameter set to 0.01. Greater smearing during relaxation was used to achieve faster convergence. The convergence threshold was 1e-7 Ry. After that, non-self-consistent field (NSCF) calculations were performed on a $10 \times 10 \times 10$ grid with the tetrahedron method for Brillouin zone integration for density-of-states (DOS) calculations.

The Maximally Localized Wannier Functions (MLWFs) were calculated via Wannier90 v.2.1.0 software[22]. First, NSCF calculations were performed with QUANTUM ESPRESSO on a 64 k-point grid with *nosym* and *noinv* flags both equal to *true*. After that, Wannierization was performed with automatic projections via the SCDM-k method[23]. The threshold for conduction bands deconvolution was 1e-11, with the maximal number of deconvolution iterations equal to 1000. Only 1e-6 was reached. The increase in the number of iterations up to 3000 led to a convergence of 1e-8, but did not significantly affect the final total spread of Wannier functions. Therefore, to optimize computational efficiency, the initial 1000 iterations were retained.

Additional calculations were performed for B1, particularly the Hubbard U correction, which was included to account for onsite Coulomb interactions for localized orbitals. The value of U was set in the range of $0 - 8$ eV for the d states of Hf. Only one effective parameter is used, omitting the multipolar terms[24].

The influence of spin-orbit coupling was considered for B1. Owning to the high computational cost, calculations were not performed for T1. The structure was first relaxed with the 'vc-relax' option in the Γ point only. For the SCF and NSCF steps, the grid was chosen the same as for non-spin-orbit calculations. Notably, approximately 100,000 h of computational time (number of cores multiplied by run time) on the cluster was necessary to perform spin-orbit calculations (SCF and NSCF steps), whereas only 5000 were needed for calculations without it.

The electronic transport properties were calculated from the band structure via BoltzTraP v.1.2.5 software[25] (URL: https://www.tuwien.at/en/tch/tc/theoretical-materials-chemistry/boltztrap). The maximal k-point grid involves an $30 \times 30 \times 30$ mesh. The same density mesh was used to reconstruct the Fermi surface.

All figures, including the figures in the Supplementary Information, were prepared by the authors with Microsoft Office 16 PowerPoint (URL: https://www.office.com/) to combine individual charts into one object; Blender v. 4.1 (URL: https://www.blender.org/) to create 3D models; MATLAB R2024a (URL: https://www.mathworks.com/products/matlab.html) to generate chart data and isosurface plots and FermiSurfer 2.4.0 (URL: https://mitsuaki1987.github.io/fermisurfer/) to plot the Fermi surface.

Results

Structural relaxation

The structure after relaxation has a lattice constant equal to 14.3185 Å for B1 and 14.3004 Å for T1. This value is almost 5% greater than the experimentally determined value 13.6740 . With the GGA, the overestimation of the lattice parameters is approximately a few percent, especially for the 4d and 5d states containing transition metals like Hf, which is due to delocalization[26,27]. The other reason is that the inner dodecahedron in the B-RTH cluster should not be fully occupied. Model B1 is presented in Fig. 2, whereas T1 is presented in Fig. 3.

The short distance makes Mg12 and Mg4 diagonally displaced. The distance is ~ 2.5 Å. In contrast, the nearest neighbor distance between Mg atoms in Zn-Mg alloys such as Zn_2Mg and $Zn_{11}Mg_7$ is approximately 3.0–3.2 Å[28]. There are reports that bonds are shorter than usual[29]. The short Mg-Mg bond is not the result of the elimination of mixed sites. As shown in Table 1, the simultaneous presence of Mg4 and Mg12 must occur when the total occupancy by Mg is greater than 1. Zn15 atoms fully occupy the vertices of soccerball in B1. Those atoms are displaced from soccerball vertices because they need to avoid their periodic copies. After displacement, the distance between Zn15 atoms is ~ 2.5 Å, which is standard. In T1, the Zn15 atoms shown in Fig. 3 are outside of the soccerball polyhedron. The distance from Zn15 to the present Zn14 atom is equal to 2.61 Å. The last observation is the radial displacement of Mg12 caused by the relaxed Zn atom from the inner dodecahedron in B-RTH. The Zn atoms in the 8i Wyckoff sites, called Dod1, are radially displaced from the center. The distance between the nearest Zn atoms in the inner dodecahedron is approximately 2.4 Å, which is reasonable. Dod1 atoms form a cube, whereas Dod2 atoms are mostly inner atoms arranged in an icosahedron.

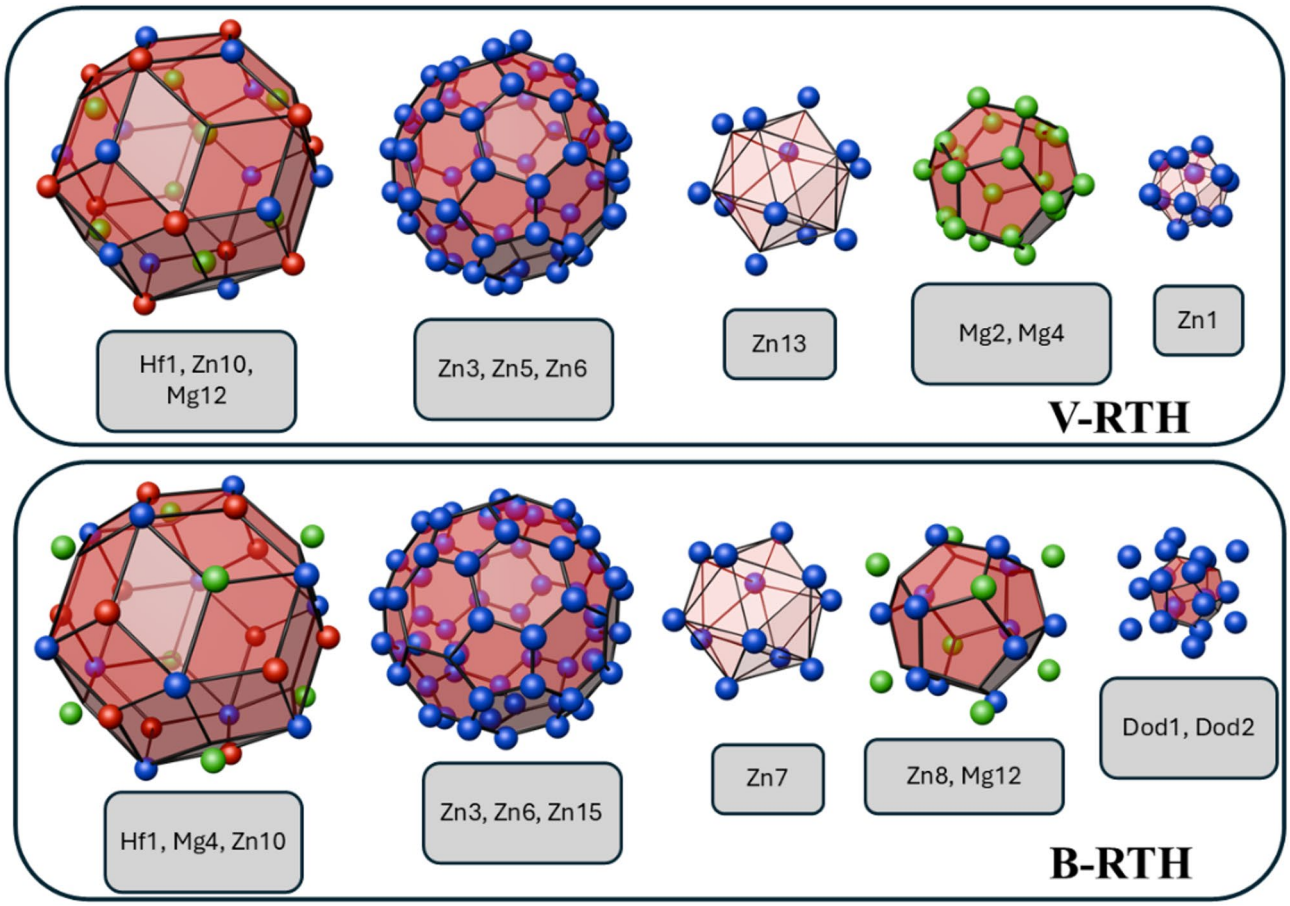

Fig. 2. Model of B1 after variable-cell relaxation. The colors are the same as those in Fig. 1.

Total energy and DOS

The total energy for B1 is higher than that for T1 by 10.9 meV per unit cell. It is highly expected that the atom from the Zn15 site will phason flip[30] to Zn14, and vice versa, even at low temperatures. The energy required for such a flip is in the range of optical phonon modes. On the basis of simulations and measurements performed on Zn-Mg-Sc quasicrystals and periodic approximant crystals, the energy of the optical modes can reach 25 meV[31,32]. Even though the energy range available in Zn-Mg-Hf can be smaller because of the higher mass of Hf, it should still be above the required energy difference. Another example of localized atomic jumps is observed in Zn- and Cd-based crystals and involves symmetry-breaking tetrahedrons[33]. This agrees with the observation that in Zn-Mg-Sc 1/1 cubic approximant crystals, the p orbitals of Zn_4 are tetrahedrally hybridized without the addition of orbitals from neighboring atoms near the Fermi energy[13].

In Fig. 4f, the relationship between the total electron energy E and the Fermi energy E_F is shown against the value of the Hubbard coefficient U. Both energies monotonically increase up to $U = 8$ eV, which is the highest considered value. The interpretation of this behavior is related to how Hubbard correction treats electron-electron interactions by increasing localization. First, the increase in the Fermi energy suggests that the density of states (DOS) in the conduction band increases making less available states in the valance band. It is well represented in Fig. 4a and d), where the highest peak for unoccupied states is shifted to a higher energy range and the peak below a pseudogap disappears. As is known from previous electronic structure calculations[34–36] and experimental work[37], hybridization is an important phenomenon in quasicrystals. With more localized d orbitals due to Hubbard correction, the hybridization is weaker, resulting in higher energies. The same reasoning is applicable for the total electron energy. With weaker hybridization, the formation of bonding molecular orbitals is hindered, resulting in higher total energy. A more detailed analysis of the band structure resulting from the addition of Hubbard correction is performed in Supplementary Sect. 1. In Supplementary Fig. S1 the band structure for the B1 model with $U = 8$ eV and no Hubbard correction is shown. The impact of the orbital bonding/antibonding configuration on the dispersion relation is determined on the basis of of the decomposition of two Kohn-Sham states into atomic orbitals as shown in Supplementary Fig. S2.

In Fig. 4c, the DOS was calculated on a higher density mesh of k-points. The mesh was $9 \times 9 \times 9$ for the SCF step and $18 \times 18 \times 18$ for the NSCF step. The difference is qualitatively small.

The role of Mg in stabilizing the structure remains unclear. From DOS plots, Mg states play a marginal role in bond formation, as the DOS is uniform across a wide range of energies, excluding deep states at approximately -8 eV, with E_F being a reference energy (Fig. 4b). They do not participate in the formation of the pseudogap

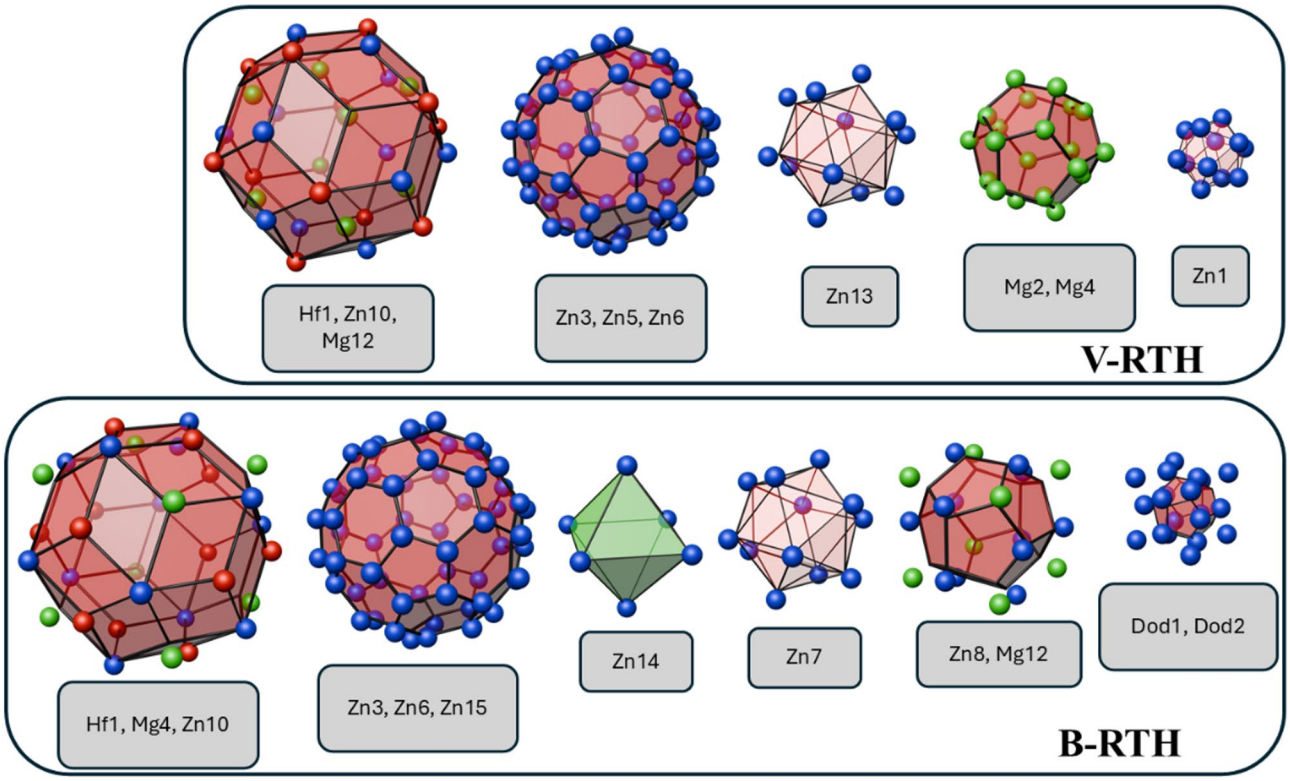

Fig. 3. Cluster shells of model T1 after variable-cell relaxation. The colors are the same as those in Fig. 1.

that is considered crucial for quasicrystal stabilization. Upon closer examination, it can even be seen that the Mg-3s states have a dip in the DOS at approximantely − 1 eV. The DOS increases in the span of the pseudogap, reaching a maximum at the Fermi level that remains unchanged until the end of the pseudogap. In the context of 1/1 Zn-Mg-Sc, similar conclusions could be drawn regarding the role of Mg in the pseudogap formation[13].

The introduction of spin-orbit coupling does not result in a substantial change in the DOS. The shape of the DOS in Fig. 4e is qualitatively the same as that in Fig. 4a. The higher energy states are cut out to limit the memory requirement. The detailed structural analysis will therefore be executed with $U = 0\,\mathrm{eV}$ and no spin-orbit coupling. However, spin-orbit coupling will be invoked when the formation enthalpy is considered.

LDOS

In this section, we investigate the difference in the local density of states (LDOS) resulting from the insertion of the Zn14 atom into the structure. Figure 5 shows the local structure of 1/1 Zn-Mg-Hf around Zn14. The coordinates of the Zn7 and Zn8 atoms move slightly inward and outward of Zn14. The most significant change concerns the Zn15 atoms. For B1, the top Zn15 atoms come from the periodic copy of the unit cell. In T1, Zn15 atoms are located exactly at the unit cell face. The distance between Zn15 located on the soccerball shell and Zn10 from the triacontahedron decreased from 3.2435 Å to 2.8573 Å. On the other hand, the distance between Zn7 and Zn15 increases from 2.5125 Å to 3.2163 Å. The nearest distance of the Zn14 atom to neighboring Zn is equal to 2.5056 Å, which is still chemically acceptable. The Zn-Zn bond length in $Zn_{11}Mg_2$ is approximately 2.56 Å, whereas it can be even smaller in molecular crystals[38]. The distance between Zn15 and Hf1 decreases from 3.3408 Å to 3.2772 Å. The impact of hybridization can therefore be expected to increase.

Let us first discuss the impact on Hf-5d states. There is only a subtle change around the Fermi level (Fig. 6). The local peak around the Fermi energy is smeared out for T1, and the LDOS formes a continuous slope up to the peak at 2 eV. The increase in the LDOS of Hf-5d states at −7.7 eV correlated with the increase in the LDOS for Zn-4p states for the same energy visible for all presented Zn atoms (Figs. 7 and 8). It is possible that the hybridization of Zn-3d states with Hf-5d plays a role as it is in the same energy range. However, the greatest change concerns Zn15 atoms, which confirms the increase in hybridization between the Zn15-4p and Hf1-5d orbitals.

A subtle change in the LDOS occurs for Zn6 and Zn7 (Fig. 7). The peak at the Fermi level is still present in both cases, although the width of the peak increases for T1. The width of the pseudogap is the same, and the heights of the peaks around the Fermi level for the occupied and unoccupied states are slightly modified. The same trends are observed for both the p and s orbitals. It can be concluded that there is a weak interaction between Zn14 and those atoms.

The story is different for Zn15 (Fig. 8). Apart from the previously mentioned peak increase for deeper states around the d orbitals of Zn, a peak at the Fermi level appears. Its height is as large as the depth of the pseudogap. It solely concerns p states, and it is not related to transfer from s to p orbitals, as the LDOS for s states also

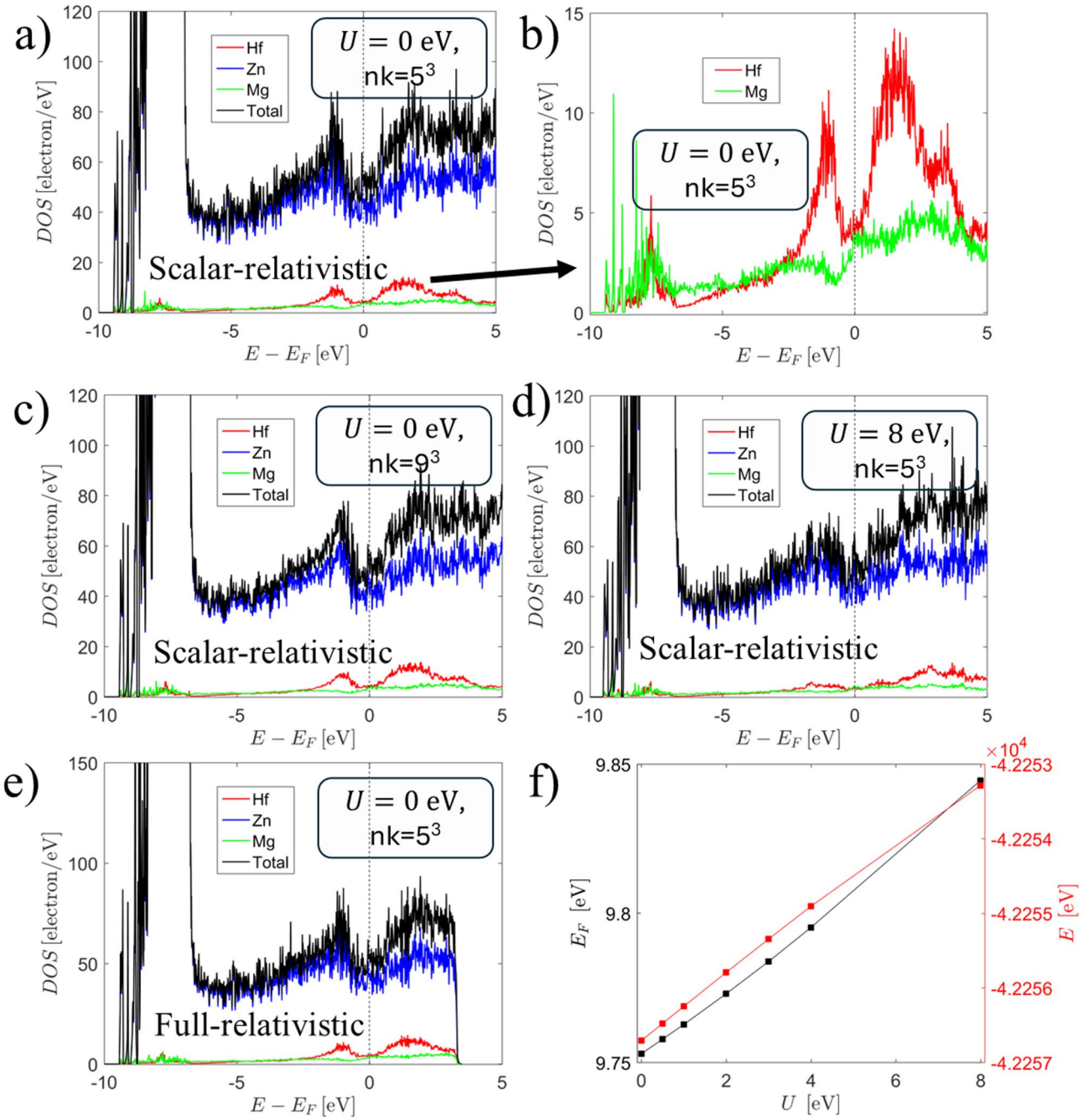

Fig. 4. (**a**–**e**) DOS calculated for B1 (**a**–**e**); (**f**) dependence of the total energy E and Fermi energy E_F with respect to the Hubbard coefficient U. The plot for (**c**) has the same parameters as a) except for the denser k-point grids for the SCF ($9 \times 9 \times 9$) and NSCF ($18 \times 18 \times 18$) steps. (**b**) Magnified Mg and Hf states of (**a**) are shown.

increases. The increase in the peak height at the Fermi level is related to the decrease in the LDOS of unoccupied states, in particularl, more bonding Zn15 p_y-Zn15 p_y σ bonds are formedz as discussed in Supplementary Sect. 2. Additionally, weaker bonds between p_z orbitals occur due to the absence of periodic copies of Zn15. The shift in the LDOS for a particular orbital is shown in Supplementary Fig. S3.

The qualitative difference is also evident for the LDOS of Zn8. The deep, narrow pseudogap visible in B1 is absent in T1 (Fig. 8). Instead, it appears to be a broad valley with a mild slope for unoccupied states. A detailed analysis of the projected DOS, as presented in Supplementary Sect. 2, indicates that p_x orbitals play a crucial role as Zn14 interrupts the formation of σ bonds between Zn8 atoms.

The general conclusion coming from DOS analysis is that the stability of a specific formation is governd by p orbitals whereas d orbitals of Hf form a stable backbone of the structure.

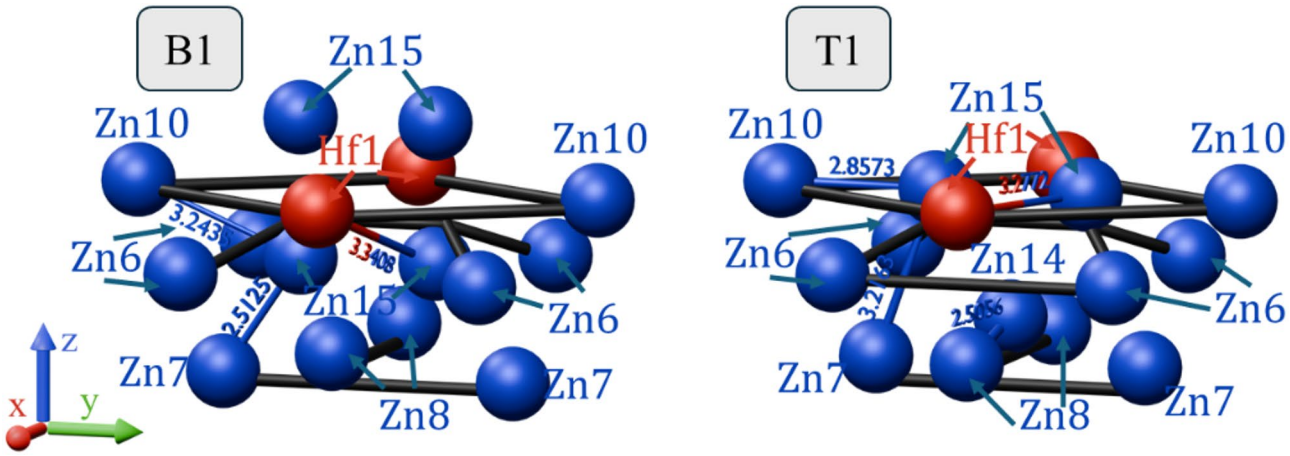

Fig. 5. Local atomic environment around the Zn14 site.

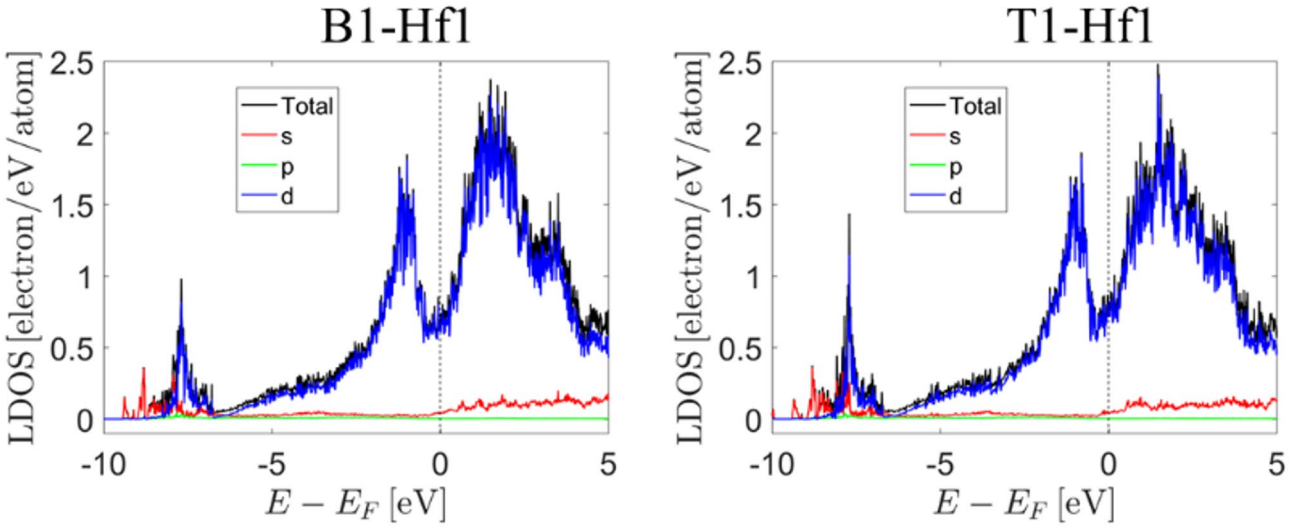

Fig. 6. LDOSs of Hf1 atoms for the B1 and T1 models. The peak near − 7.7 eV is more prominent for T1.

Charge distribution analysis

In our analysis of the charge distribution, we use Löwdin population analysis[39]. The method is more resilient than the popular Mülliken analysis[40] because of the use of an orthogonalized basis set. Löwdin partial charges are compared to Bader charges[41]. The Bader population analysis is executed with the software developed by Henkelman et al.[42,43].

The bonding characteristics of metallic alloys can be complex with topological features[44,45]. The analysis of charge transfer in the Zn-Mg-Al-Li system revealed preferential site occupancy by electropositive and electronegative elements[46]. Site preference was also detected in Zn-Mg-Sc[13] and Ag-Cd[47] systems, which are closely related to quasicrystals. Even though quasicrystals and approximants are not Zintl phases[48,49] and all the experimental evidence suggests that they are Hume-Rothery phases[50], the local charge transfer and formation of nonmetallic bonds help stabilize the complex structure.

The visualization of partial charges is presented in Fig. 9, where the electronegative sites are plotted in blue and the electropositive sites are plotted in red. Only the asymmetric unit is shown for clarity. The radius of a sphere is proportional to the partial charge. The specific values of the charges can be found in Supplementary Table 1. The electrons occupying the s, p and d orbitals for Löwdin charges are separated.

The leading role in charge transfer is played by the Zn-4p, Zn-4s, Mg-4s and Hf-5d bands. The highest charge transfer occurs for Mg atoms, resulting in a positive charge in the range of (+ 1.43, + 1.57) in terms of the Löwdin charge. The Bader charges for Mg12 and Mg4 are relatively low, at approximately + 1. The difference between the charge analysis results indicates the presence of localized electrons that are attributed to the p states of Zn. The highest charge is observed for Mg2, which is not in direct contact with another Mg atom. No localization for Mg2 is indicated by the Bader charge, as the values are similar for both computational methods. The charge for Mg12 and Mg14 is high even though their interatomic distance is small. For $Mg_{29-x}Pt_{4+y,}$ agglomeration

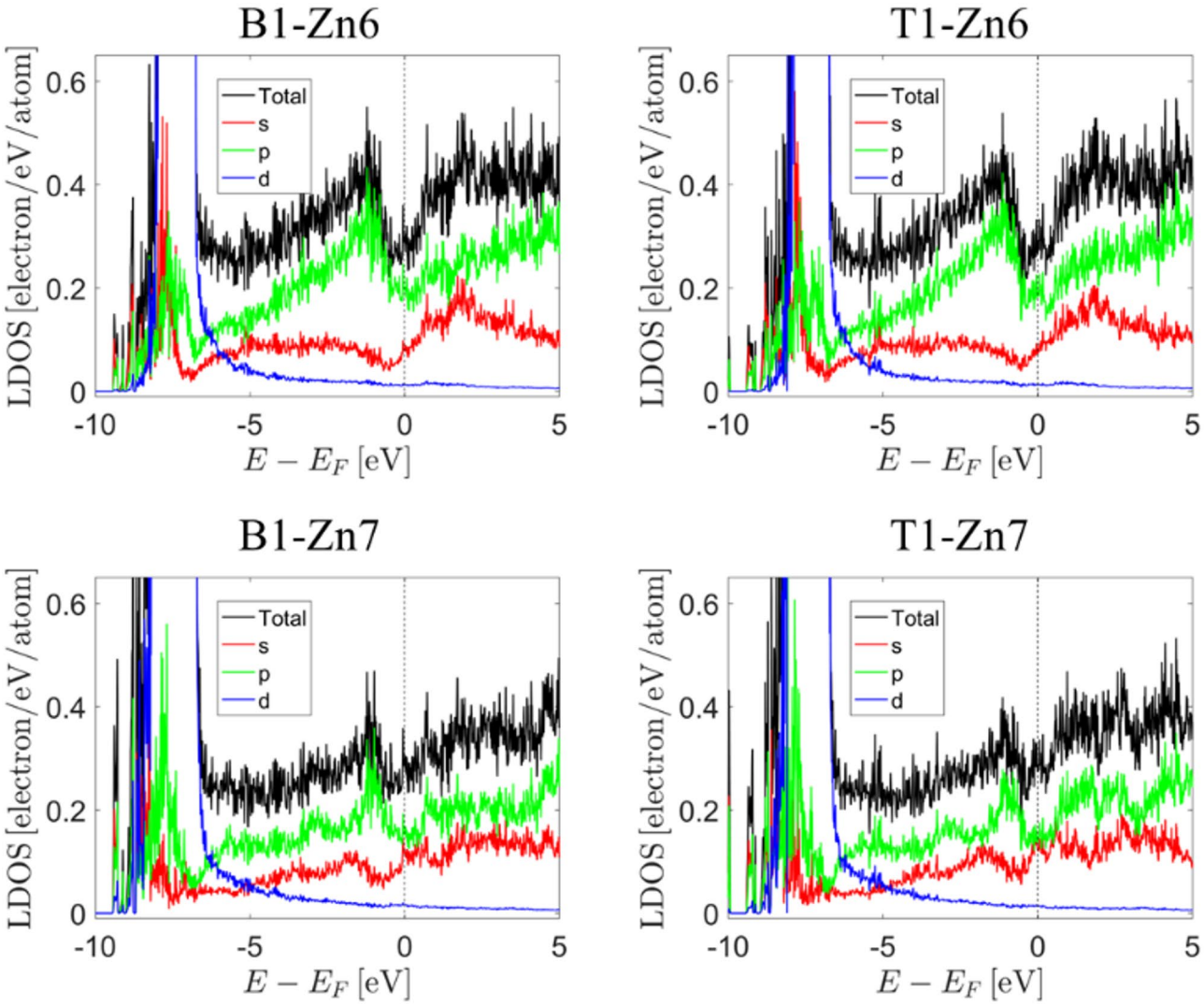

Fig. 7. LDOSs for Zn6 and Zn7 atoms for the B1 and T1 models.

of electropositive atoms in one region can lead to an unfavorable distribution of charge, resulting in Mg atoms being even negatively charged[51]. In terms of the negative charge, the highest charge is placed on Zn1, and the second highest charge occurs for Zn13, independent of whether the B1 or T1 model is considered. Both are atoms belonging to V-RTH shells. A fractional or even positive charge is observed for the Zn atoms of the B-RTH cluster. The positive charge for Zn7 was confirmed for both population analyses. The transfer of electrons can therefore be linked with the increased stability of the V-RTH cluster. Compared with other atoms, the charge surplus for Zn1 and Zn13 concerns both the s and p orbitals. The highest charge on the p orbitals for Zn outside of the mentioned two is −1.7428 for Zn3 in T1, whereas for Zn13 and Zn1, it is −1.9064 and − 2.0555, respectively.

The greatest change in the electric charge between B1 and T1 occurs for Zn15 and Zn8 because of the introduction of the Zn14 atom. The charge for all of them is small, which is a sign of too high agglomeration of electronegative atoms in the sense of Pauling's second structural principle[52]. In a real structure, the variation in electronegativity is provided by the inclusion of Mg in Zn10 and Zn8. Notably, in the electronic structure of 1/1 Zn-Mg-Sc, the position of Zn14 could be occupied by an electropositive atom balancing the charge distribution[13].

The Madelung energies for both models are computed as a measure of Coulomb interactions. This method was useful for predicting the valance band of bismuth-containing layered structures[51] or the stability of $Ag_{34}Te_{21}$[53]. It is also a measure of the lattice energy for ionic compounds with a linear dependency relationship[54]. The calculations for both models were performed in VESTA v.4.6.0[55]. Each Löwdin partial charge was assigned to the corresponding atom. The ionic sphere radius was chosen as 1.1 Å (less than half of the smallest interatomic distance), and the reciprocal space range was set to 5 $Å^{-1}$. The calculated Madelung energy is −10.903 eV for T1 and − 10.429 eV for B1. Different choices of ionic sphere radius do not change the conclusion. The lowest Madelung energy is calculated for T1, which is consistent with the total electron energy being lower. Our models have the same stoichiometry; therefore, the total electron energy for both of models is the same as that for the formation enthalpy. For formality, we calculated the formation enthalpies for B1 to be 5.271 kJ/mol and 5.265 kJ/

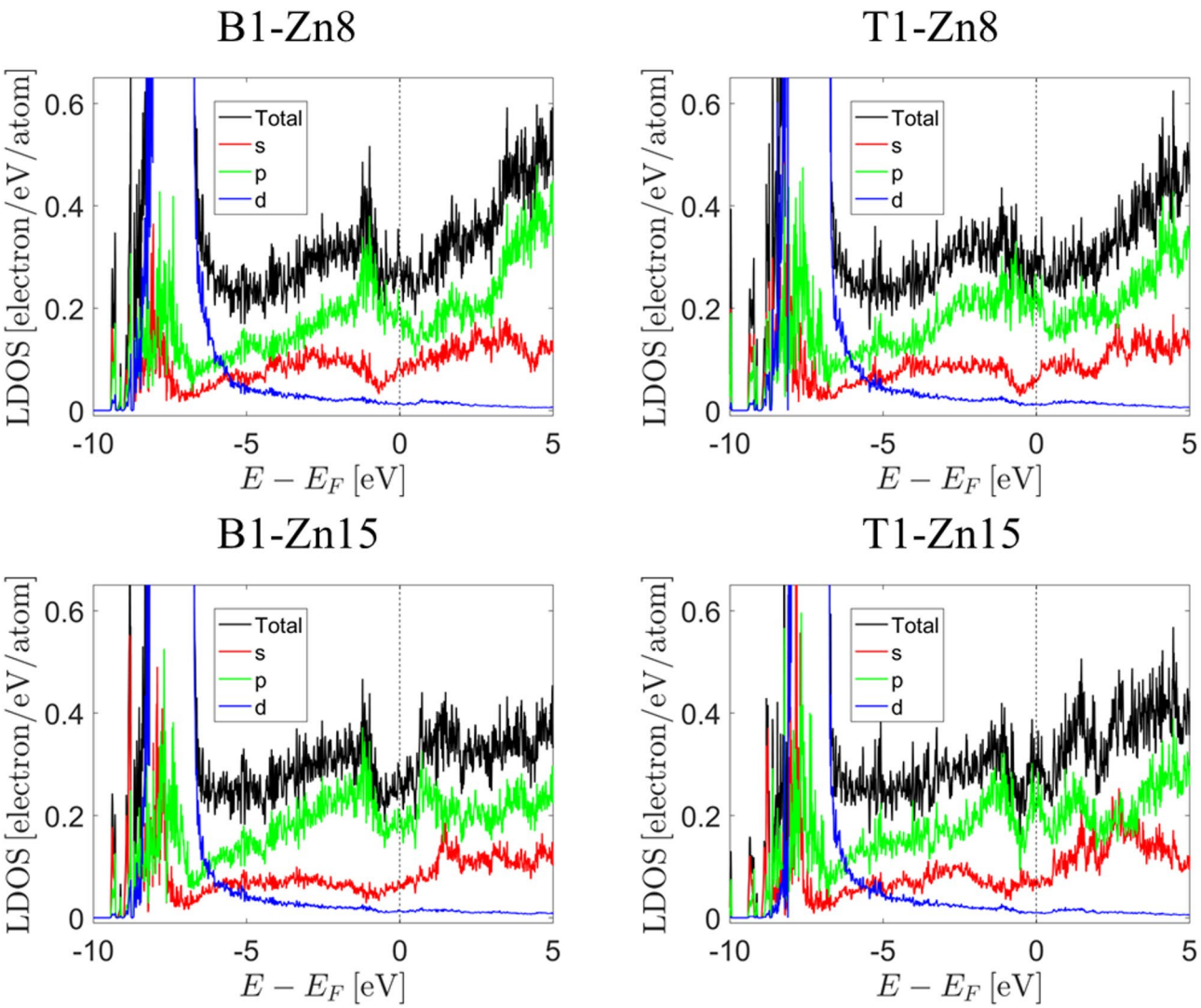

Fig. 8. LDOSs for Zn8 and Zn15 atoms in the B1 and T1 models. The primary feature is the disappearance of the pseudogap for Zn8 due to the smaller DOS for the s orbitals. In the case of Zn15, the peak for the Fermi energy arises.

mol for T1. We used a standard formula for the formation enthalpy, which is valid at the limit of pressure being close to zero. The formula for the formation enthalpy is as follows:

$$\Delta H = E - \sum {}^{N}_{i=1} N_i E_i, \tag{1}$$

where E is the total electron energy, N_i is the number of i atoms, N is the number of atomic species in the structure and E_i is the total energy per atom calculated for the elemental reference state. All the structures of individual atoms were hexagonal structures with $P6_3/mmc$ space groups and two atoms per unit cell[56]. The structures were relaxed prior to the SCF calculations. The specific parameters for the formation enthalpy calculations are given in Table 2. The formation enthalpy is positive, indicating that 1/1 ZnMgHf is an endothermic compound. Only the inclusion of spin-orbit coupling determined the structure to be exothermic. It is therefore important for predicting phase stability.

The necessity of introducing spin-orbit coupling to correctly predict phase stability apparently contradicts our earlier statement that it can be omitted in subsequent experiments oriented toward revealing the nature of electron bonds. We would like to emphasize that the scalar-relativistic approach in terms of chemical bonds and DOS was shown to be accurate enough to make the results meaningful. The DOS does not change with the addition of spin-orbit coupling, as shown in Fig. 4a, e. In Sect. 4. Figure 18 shows that the calculated conductivities for both the scalar and fully-relativistic approaches overlaps, indicating that the band structure is not altered. The spin-orbit coupling can therefore be omitted for bonding analysis but is important for correctly predicting the phase stability, especially because the formation enthalpy is small.

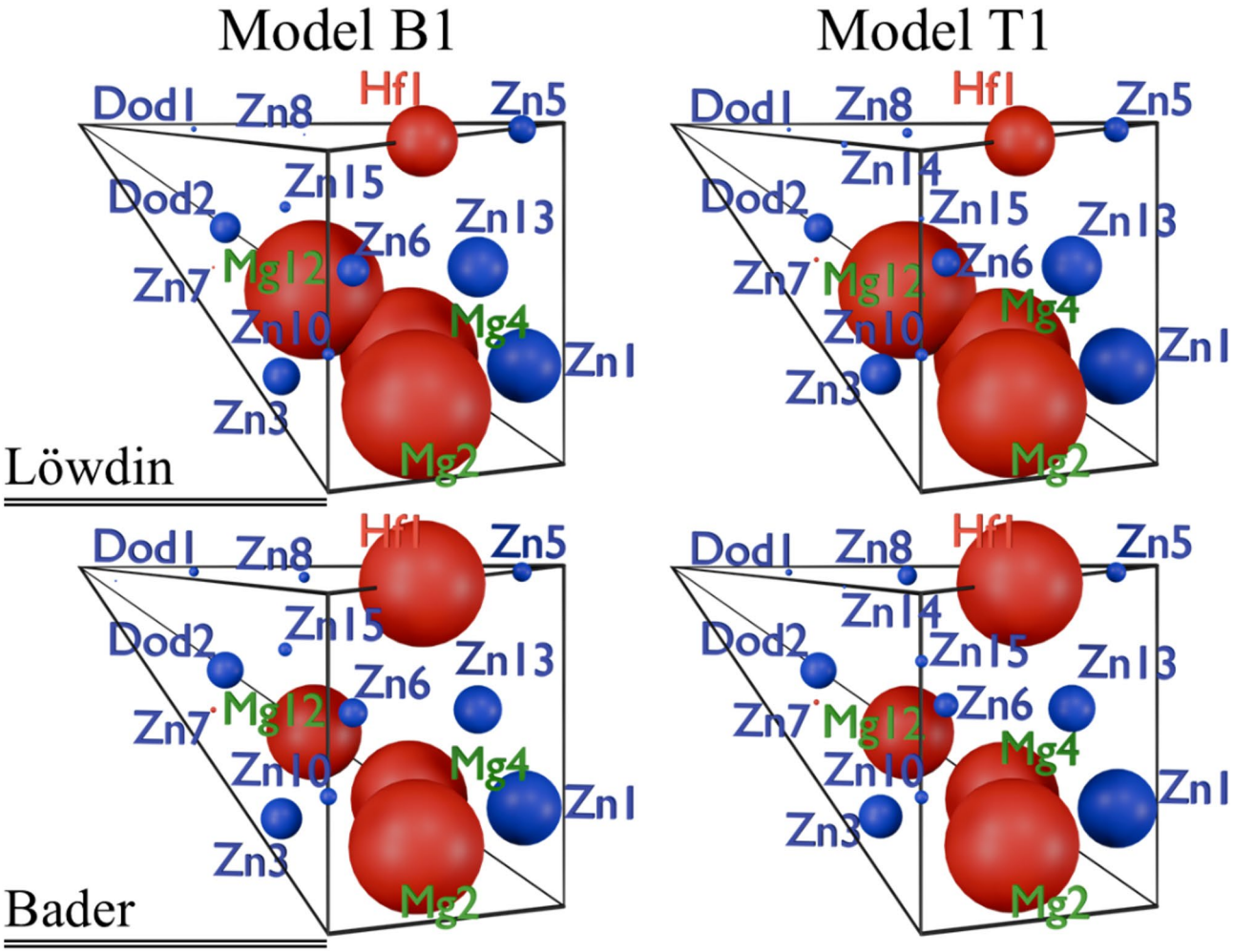

Fig. 9. Löwdin and Bader partial charges plotted in the asymmetric part of the unit cell for models B1 and T1. The positive charge is plotted in red, and the negative charge is plotted in blue. The size of the sphere is proportional to the partial charge.

	B1	T1	Zn	Mg	Hf
Lattice parameters [Å]	$a = 14.31847$	$a = 14.30042$	$a = 2.7371$ $c = 4.48653$	$a = 3.17207$ $c = 5.16350$	$a = 3.19390$ $c = 5.00546$
Energy [Ry]	-42256.709166 -42309.486014*	-42256.709969	-487.443294 -487.811672*	-282.790067	-1392.438756 -1401.077653*
ΔH [kJ/mol]	T1	5.2653 kJ/mol			
	B1	5.2713 kJ/mol -2.8298 kJ/mol*			

Table 2. Computed total energy for B1 and T1 with the given elemental crystal structures. *Energy with spin-orbit coupling.

Electron localization function

Bond analysis can be performed via an electron localization function (ELF), which is a measure of the electron localization in a picture of the pair probability density[57,58]. The topological aspects of ELF are helpful for analyzing the complexity of bonds in metallic solids (e.g.[59–61]). The distribution of attractors in interstitial regions is particularly promising for predicting the structure even under pressure[61].

In Fig. 10, we present the first noncore attractor to develop for ELF = 0.53 in B1. Three attractors are positioned between the Mg4 and Mg12 atoms in the plane perpendicular to the bond. Starting from ELF = 0.5, subsequent attractors are visible in the plane of the hexagonal ring formed by the Zn6 and Zn3 atoms. Another attractor arises in the geometric center of the tetrahedron formed by Mg4 and three Zn1 atoms. In the combined domain presented in Fig. 10, the integrated charge is approximately 0.2e. The analysis of ELF correlates with the disparity

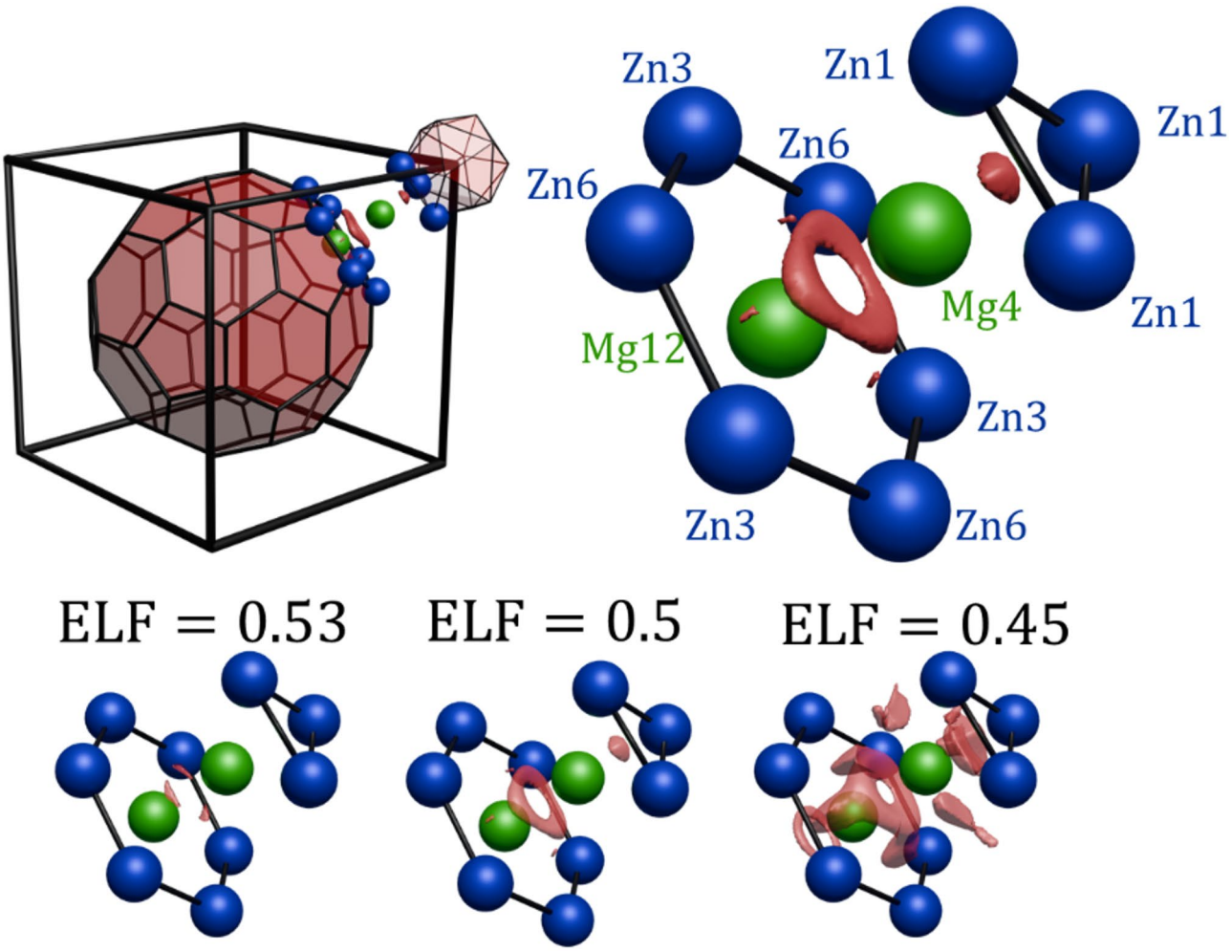

Fig. 10. The local environment of the highest valance attractors of ELF. The strongest localizations occur in the neighborhood of Mg12 and Mg4 in the plane of the soccerball polyhedron face.

between the computed Bader and Löwdin charges of Mg4 and Mg12. The existence of a polysynaptic basin with a low basin population is a clear indicator of multicenter metallic bonding[62]. The highest valance attractors are located inside the V-RTH cluster, which shows the least positional disorder, emphasizing the role of the local concentration of electric charge in structural stability. The isosurface for T1 is identical to that for B1.

The presence of the attractor in the tetrahedral site raises the question of more multicenter bonds in the structure. In Fig. 11, we present two sections through the ELF containing Hf1 atoms. Attractors above ELF = 0.4 are shown with silver spheres. Tetrahedral polysynaptic basins are quite common in the structure. They are homoatomic with Zn atoms and heteroatomic with three Zn atoms and Hf or Mg as the fourth atom. The addition of Zn14 changes the orientation of the bonding tetrahedron, as indicated by the V(Zn8, Zn15, Zn15, Hf1) and V(Zn8, Zn15, Zn6, Hf1) basins. In addition to attractors at tetrahedral sites, there are numerous trisynaptic basins. The addition of Zn14 increases the number of three-center bonds. As indicated by Fig. 10, numerous local maxima of ELF occur around Mg atoms. Multiple maxima are found around Hf atoms due to the strong delocalization of electrons.

We also performed the analysis of noncovalent bonds on the basis of the paper by E. R. Johnson et al.[63]. This result indicated the repulstive behavior in the center of B-RTH and the Zn14 site, which is empty in B1. More details can be found in Supplementary Sect. 4. In Supplementary Fig. 4 the region of repulsive force due to steric conditions is presented.

Maximally localized Wannier functions

MLWFs can be used to derive the nature of chemical bonds[64]. In the context of quasicrystals and their periodic approximant MLWF, several Al-TM compounds have been analyzed[65,66]. In this picture, the existence of three-center bonds explains the semiconductive nature of the 1/1 Al-Pd-Co[67] modeled according to Katz-Gratias-Boudard[68–70].

The initial localized orbitals for Wannierization are found via the SCDM-k method[23]. The only parameters required for the SCDM-k method applied for entangled valance and conduction bands are μ_{SCDM} and σ_{SCDM} associated with the complementary error function

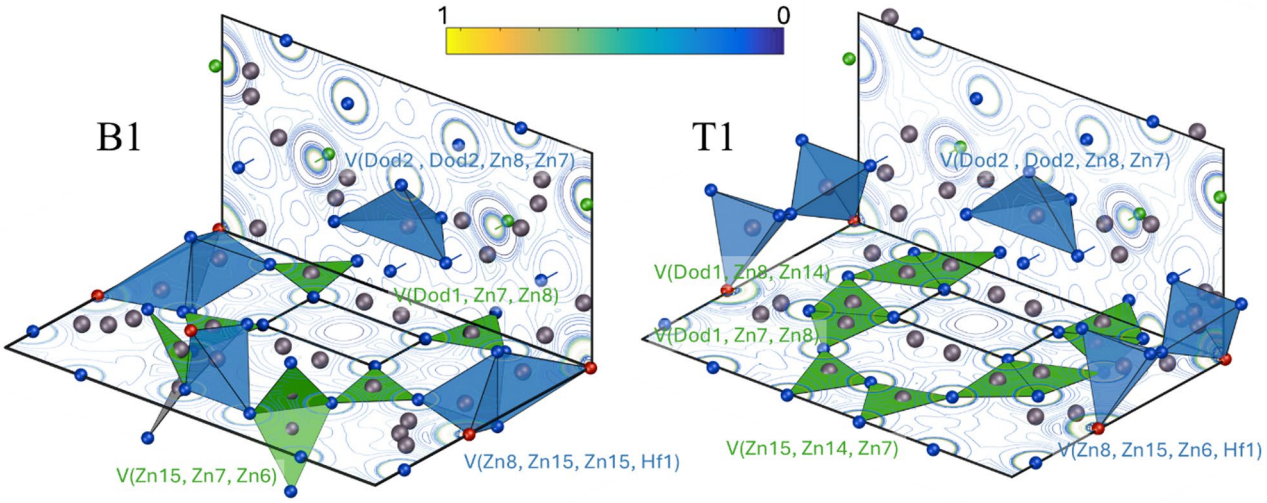

Fig. 11. Two sections through the unit cell of B1 and T1. The planes of the sections are $z = 7.3$ Å and $x = 4.3$ Å . Valance basin attractors are marked with silver spheres. Three-center and four-center bonds are highlighted.

$$f(\epsilon) = \frac{1}{2} erfc\left(\frac{\epsilon - \mu}{\sigma}\right). \tag{2}$$

According to the paper by Vitale et al.[71], the parameters of the function $f(\epsilon)$ can be fitted on the basis of the projectability of the Kohn–Sham states. The parameters for the SCDM-k procedure are then taken as $\mu_{SCDM} = \mu - 3\sigma$ and $\sigma_{SCDM} = \sigma$. The fitted function of the projectability of the Kohn–Sham states with respect to energy is shown in Fig. 12. The Wannierized band structures plotted with red crosses, as shown in Fig. 12 (right), are in perfect match with those computed with QUANTUM ESPRESSO. Wannierization is therefore successful.

The final spread parameters of the Wannierization are shown in Table 3. The dominant part of the total spread is the gauge-invariant part, Ω_I. The off-diagonal gauge dependence, Ω_{OD}, is also significant, expressing the overlap between neighboring functions. The spread of atom-localized Wannier functions is less than 1 Å^2. The higher contribution comes from off-atomic centered functions that are spread in between $5.69 - 25.69$ Å^2 . The histogram of individual Wannier function spreads is shown as an inset in Fig. 12. Since the lattice size is approximately 14.3 Å and the spread does not cross the intercell boundary, it is acceptable in the metallic system.

Figures 13 and 14 present Wannier center neighborhoods in the B1 and T1 models, respectively. The types of centers are divided into two centers, three centers and tetrahedra, each of which is marked with a different color. The MLWF analysis confirms the presence of multicenter bonds, including tetrahedral sites. For T1, Hf atoms participate in the formation of tetrahedral bonds, as seen in the ELF function. Model B1 has bonds that can be classified as two-center polarized bonds between Zn and Hf.

Multicenter bonds are more prevalent in the V-RTH cluster, especially soccerball polyhedron. The rhombic triacontahedron of B-RTH in T1 also has a tetrahedral center, but it is shared with V-RTH because of c-linkage. The existence of numerous multicenter bonds correlates with the apparent greater stabilization of the V-RTH cluster than the B-RTH cluster. The classification of Wannier centers, although prone to error due to high spread, confirms the existence of multicenter bonds.

In Fig. 15 (left) we present two local configurations of the MLWF centers around the Zn14 atom in T1. Three-center bonds are created between Zn14 and neighboring Zn atoms. Additionally, two-center bonds are identified. The local configuration can be compared with the ELF function, where three-center, polysynaptic basins are identified. The local maxima of ELF were found in a triangle with Zn7, whereas the Wannier center has accompanying Zn8 atoms. This could indicate that the two-center bond should be classified as three-center. However, the inclusion of Zn14 clearly increases the number of multicenter bonds, which can be linked with the increased stability of the structural model.

The righthand side of Fig. 15 presents archetypes of Wannier centers. Tetrahedral centers occur in multiple variants. The center with two Zn atoms can be polarized toward Zn–Zn bonds or Mg–Mg bonds. Three center bonds also occur in the variants, including three and two Zn atoms. Whenever there is a Zn–Mg bond, the center of the Wannier function is polarized toward Zn, which is a result of charge transfer. Two types of Zn–Zn bonds occur. One is polarized toward the third atom perpendicularly to the bond, and the other is an ideal, unpolarized bond. An unpolarized bond is found between Dod1 atoms in the center of B-RTH. Mg–Mg bonds are rare but occur between Mg4 and Mg12. One additional Mg2–Mg2 bond is found in the V-RTH of B1. There is one characteristic difference between the bonding characteristics of Hf atoms in the two considered models. The tetrahedral Wannier center is found along the edge of the rhombic triacontahedron and includes Zn3 and

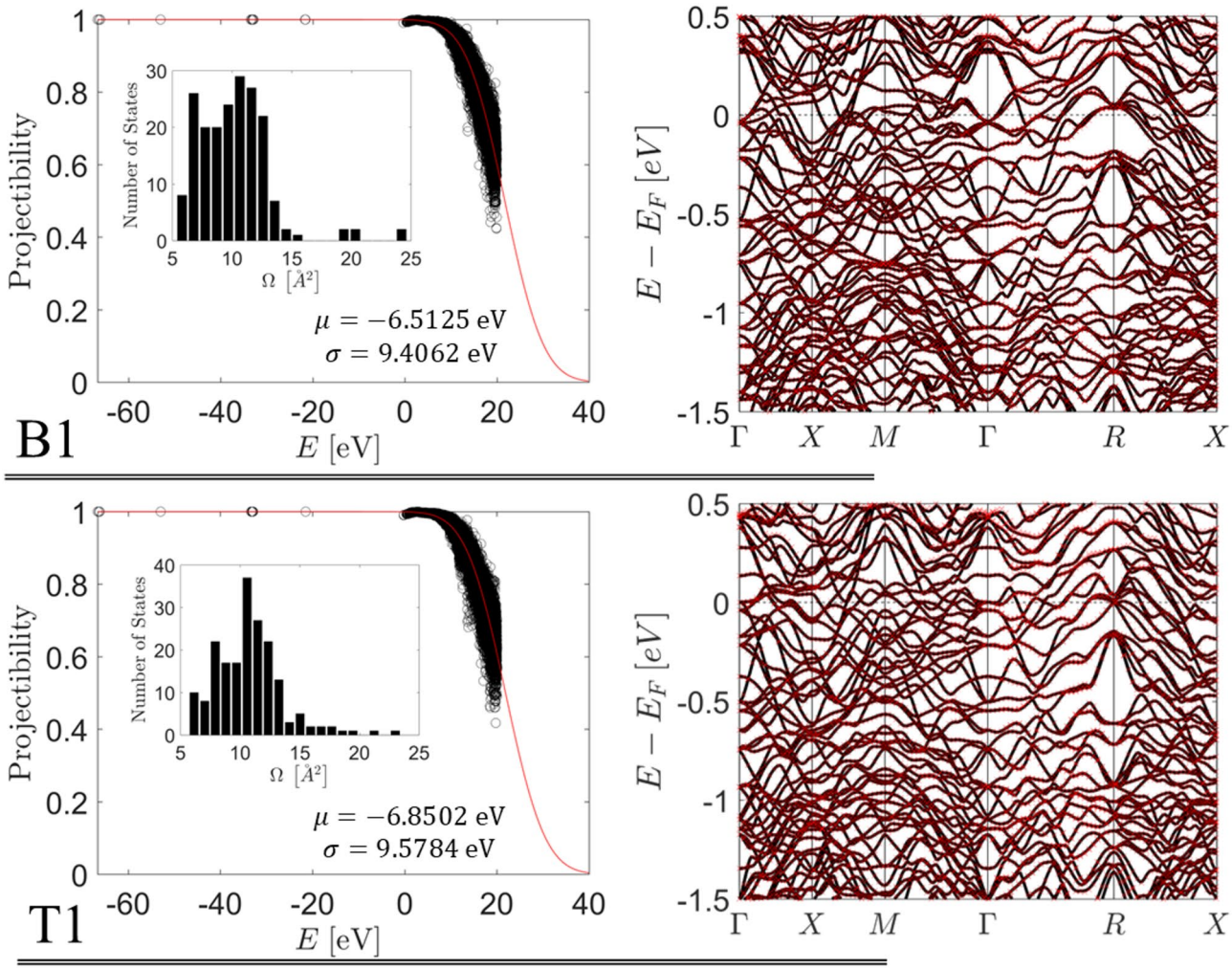

Fig. 12. (left) The projectability vs. energy plot for B1 and T1 for determination of the coefficient for the SCDM-k procedure. The distribution of individual MLWFs is shown in the inset. (right) Band structure plot for the original data (black) and after Wannierization (red). The ideal agreement is shown.

	Ω_I	Ω_D	Ω_{OD}	Ω_{Total}	N_{bands}	N_{NA}
B1	2234.3884	0.5835	894.6469	3129.6189	884	192
T1	2260.1774	0.7337	896.0361	3156.9472	883	191

Table 3. The parameters after Wannierization with the Wannier90 code. The total number of bands below or crossing the fermi level is equal to N_{bands}, among which N_{NA} are not centered at atoms.

Zn5 atoms. This is only found for T1. The two-center bond of Zn–Hf is directed toward individual atoms from soccerball polyhedrons such as Zn3 or Zn6. The change in the bonding character is caused by Zn14, as each Hf atom is in close proximity to Zn14. The distance is equal to 3.71 Å but is equal to the size of the MLWF spread.

Fermi surface

The electronic structure resilience to perturbations is related to the dynamical susceptibility, which can show singularities for values of the perturbation wavevector $\mathbf{q}$. In particular, a singularity appears in the case of a nested Fermi surface and is recognized as the primary cause of charge density wave formation[72]. The coexistence of a periodic approximant phase and a quasicrystal raises the question of whether Fermi surface nesting is responsible for quasicrystal formation. The Fermi surface was previously obtained for several Al-based periodic approximant crystals, but it was never analyzed with respect to the nesting effect[73,74].

In Fig. 16, we present the shape of the calculated Fermi surface. Plots were obtained with FermiSurfer v.2.4.0 software[75] (URL: https://mitsuaki1987.github.io/fermisurfer/). The shape of the Fermi surface is overly complex, as 10 and 9 bands cross the Fermi level for B1 and T1, respectively. On the left-hand side of Fig. 16, the entire

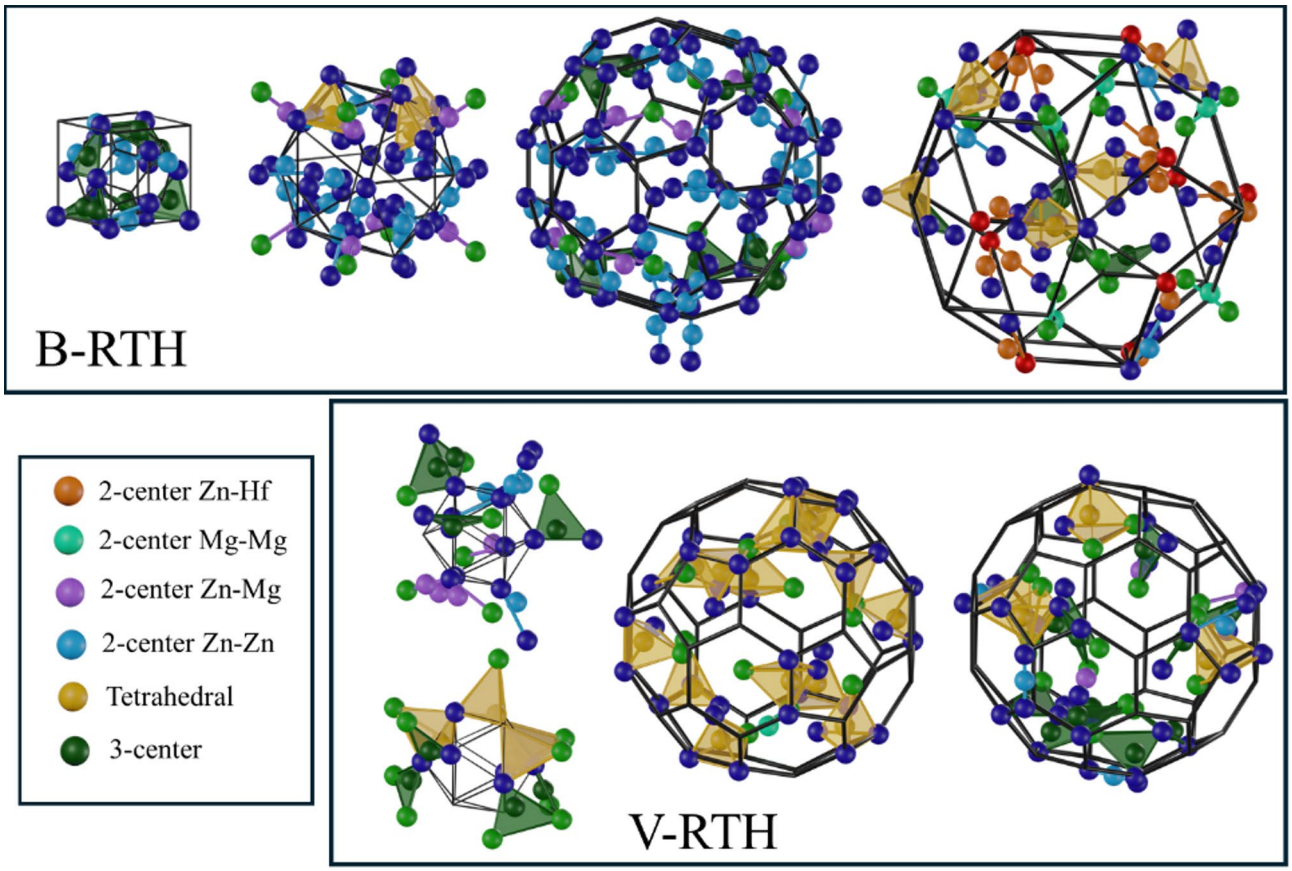

Fig. 13. The centers of the Wannier functions are divided into six types in B1. The colors of the atoms are the same as those in Fig. 1.

Fermi surface (top part) is presented with the part where significant nesting occurs (bottom part). The nesting is better visible in the 2D sections presented for Planes 100 and 101. Large parts of the Fermi surface are ideally parallel along the $\Gamma - \mathrm{X}$ and $\Gamma - M$ directions of B1. A change in nesting is observed for the T1 model. It does not occur along the direction of high symmetry but occurs along the line at $\sim 15^{\circ}$ with respect to the $\Gamma - X$ direction. Nesting occurs between bands with high-mobility electrons, as indicated by the maximal value of the Fermi velocity. The combined effect of the low energy barrier between B1 and T1 and the high mobility of electrons impacts the ease of structural transition. In addition to nesting, multiple electron and hole pockets are visible, e.g., hole pockets in the $\Gamma - X$ direction in 100 cuts of B1.

It is still unclear whether the observed feature of Fermi surface nesting is linked to quasicrystal formation. The effect of bare nesting is speculated to be insufficient for the phase transition to charge density wave structure[76]. Importantly, the momentum dependence of electron-phonon coupling[77] might be important, as electron-phonon coupling was shown to be enhanced in the quasicrystalline plane[78]. More research is necessary.

Electrical conductivity and magnetoresistance

Measurements were conducted on the icosahedral F-ZnMgHf phase. Magnetic measurements were performed with a Quantum Design MPMS3 magnetometer equipped with a 7 T magnet and operating at temperatures between 1.8 and 400 K. Only diamagnetic behavior was detected. Electrical resistivity and magnetoresistance measurements were carried out via a Quantum Design Physical Property Measurement System (QD PPMS 9T) equipped with a 9 T magnet operating at temperatures between 1.8 and 400 K. A rectangular bar sample with dimensions of $1 \times 0.8 \times 6$ mm^3 was used. The sample was grown according to a protocol published in Buganski et al. 2019[6]. A brief description of the experimental setup is given in Supplementary Sect. 5 with the sample mounted to the electric circuit shown in Supplementary Fig. 5.

In Fig. 17. The resistivity against temperature is plotted for selected magnetic fields. Metallic behavior with positive magnetoresistance is observed. It has been reported that icosahedral $Al_{62.5}Cu_{25}Fe_{12.5}$ and $Al_{62.5}Cu_{25.5}Fe_{12}$ have resistivities of $10{,}000\ \mu\Omega \cdot \mathrm{cm}$ and $4{,}500\ \mu\Omega \cdot \mathrm{cm}$, respectively, at approximately 2 K[79]. The resistivity at 300 K of the Al-W-Pd-Fe 3/2 approximants and quasicrystals is approximately $5{,}000\ \mu\Omega \cdot \mathrm{cm}$[80]. The resistivity of $Zn_{59}Mg_{29}Y_{12}$ has a minimum at 20 K, with a value of $208\ \mu\Omega \cdot \mathrm{cm}$[81]. The minimum value was also found for the Zn-Mg-Ho quasicrystal and was attributed to the Kondo effect[82]. This is not the case here, as the Kondo effect should cause the resistivity to decrease with increasing magnetic field. The low resistivity of our sample, which is approximately $46\ \mu\Omega \cdot \mathrm{cm}$, can be attributed to the high DOS at the Fermi level. The peak

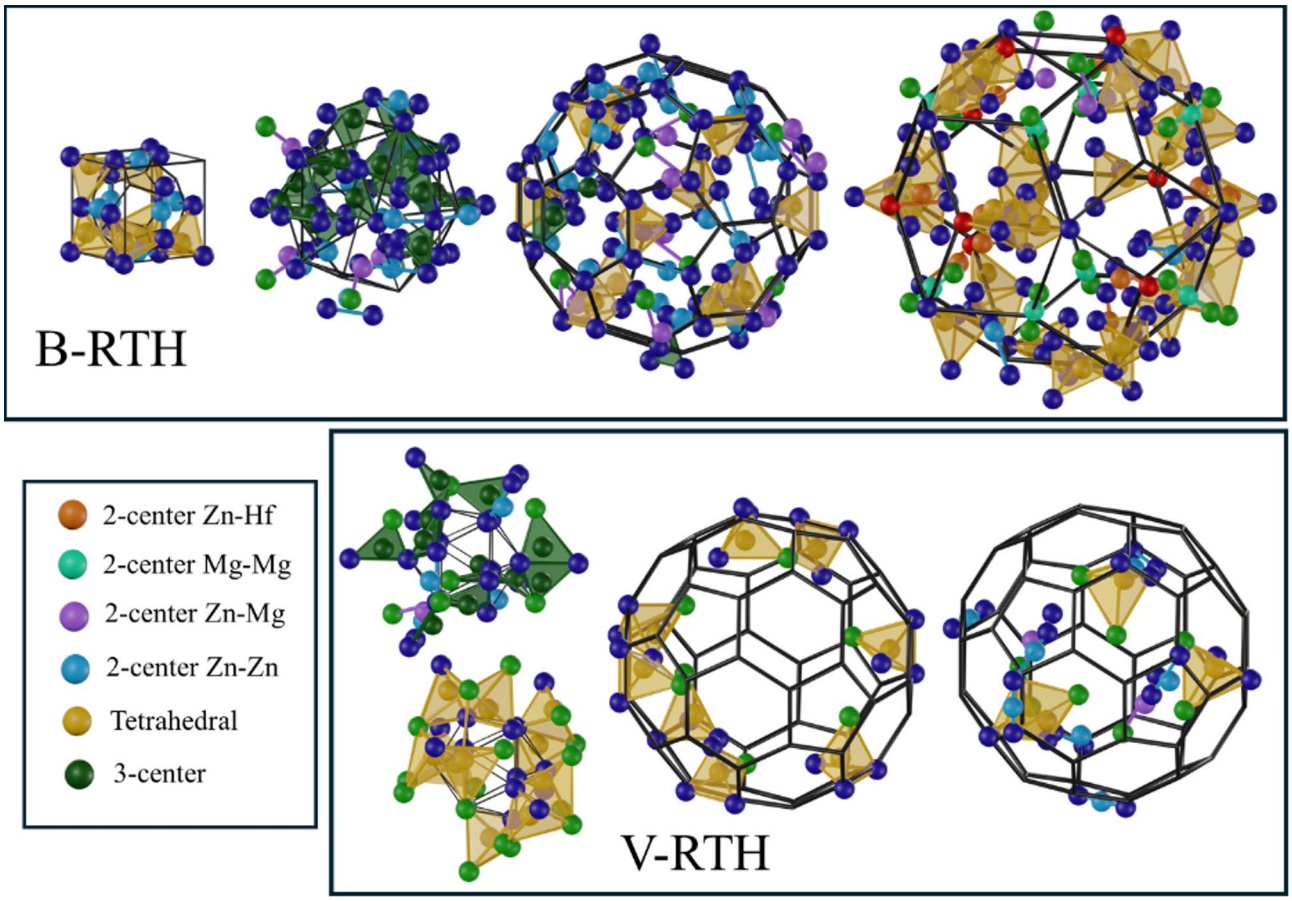

Fig. 14. The centers of the Wannier functions are divided into six types at T1. The colors of the atoms are the same as those in Fig. 1. The centers in the inner dodecahedral shell are classified as tetrahedral, although in B1, there are three centers. The distance between the centers of different classifications is approximately 0.8 Å, which is smaller than the function spread.

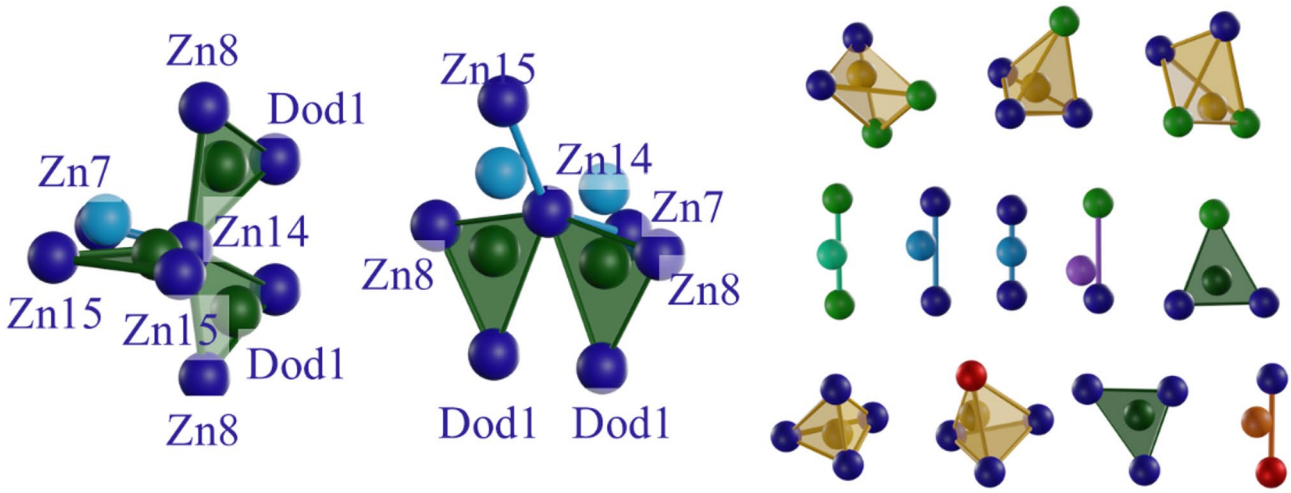

Fig. 15. (Left) Local configuration of Wannier centers around Zn14 at T1. (Right) Archetypes of MLWF centers in both models. The colors are the same as those in Fig. 17.

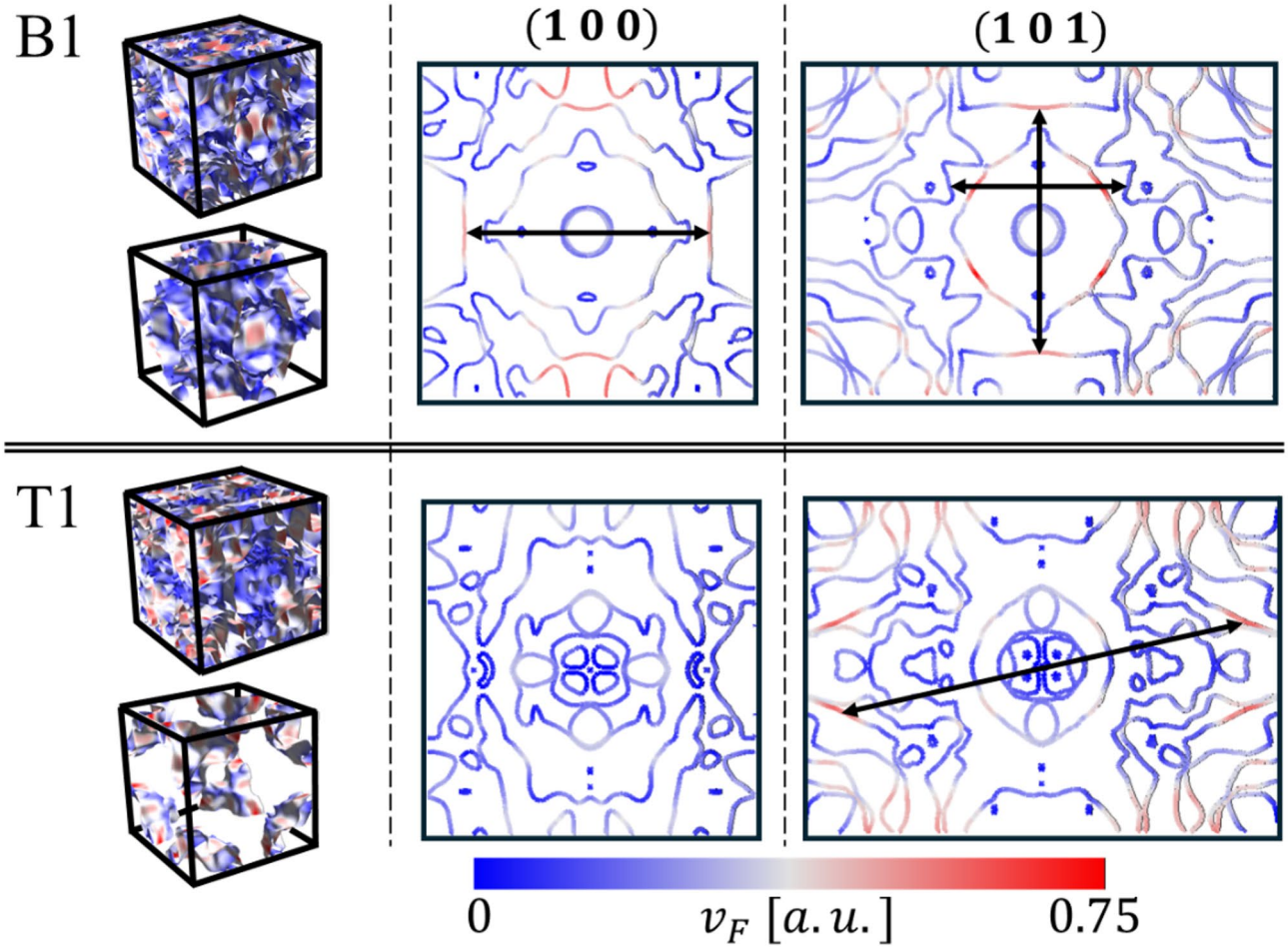

Fig. 16. The Fermi surface is 3D and presented as 2D sections in the (100) and (101) planes. The 3D Fermi surface with a nesting part is shown as the bottom part for each model. For guidance, the nesting part of the Fermi surface is connected with arrows.

in the DOS at the position of the Fermi energy increases the number of charge carriers. Al-based Mackay-type quasicrystals are known to have a deep pseudogap at the Fermi energy[83], therefore, their resistivity is higher. Fits of magnetoresistance with quantum interference effects such as weak localization or electron–electron interactions are not successful, as they are small in magnitude compared with the observed characteristics. At high temperatures (>150 K), electron–phonon scattering should dominate the resistivity. The quadratic resistivity dependence, $\rho\ (T) = A + BT + CT^2$, reproduces the shape of the experimental curve. The fitted values of the parameters weakly depend on the magnetic field. The greatest difference in the data measured at 1 T is that the resistivity was measured only at 200 K, whereas for the other data with a nonzero magnetic field, the maximal temperature was 300 K.

We analyzed the data with the theory of Boltzman transport via BoltzTraP software[25]. Figure 18 shows the conductivity and Hall coefficient for different k-meshes in the NSCF step. The difference between 25^3 and 30^3 mesh is already small, therefore, we decided to use 30^3 mesh for further studies. It was already computationally expensive to further increase the grid density. For sparser meshes, the conductivity was calculated for spin–orbit coupling with no change in curve shape. This confirms that spin–orbit coupling could be omitted in our electronic structure study. Convergence tests were only performed for the B1 model. For T1, we already use the highest-density mesh. The conductivity slightly increases with increasing temperature, except for a sudden drop at the onset of the data. The decrease in conductivity is attributed to the peak density of states at the Fermi level. For higher temperatures, states with lower DOSs contribute to conductivity. On the basis of the Hall coefficient, the conductivity is dominated by hole carriers. The theoretical observations require experimental verification.

The theoretical resistivity curve $\rho \cdot \tau\ (T)$ obtained from BoltzTraP was fitted to the experimental data (Fig. 19). The region of high temperature was selected. The only unknown factor is the temperature dependence of the relaxation time, which is approximated by a second-order polynomial. Both fits are identical. In the units of 10^{-15} s, for B1, the parameters are $\alpha \approx 16.82\,(8)$, $\beta = -2.58\,(6) \cdot 10^{-2}$, $\gamma = 3.1\,(1) \cdot 10^{-5}$. The corresponding values for T1 are $\alpha \approx 15.6\,(1)$, $\beta \approx -2.46\,(8) \cdot 10^{-2}$, $\gamma \approx 3.08\,(13) \cdot 10^{-5}$. This results in the relaxation time being equal to $1.2 \cdot 10^{-14}$ s for B1 and $1.1 \cdot 10^{-14}$ s for T1 at 300 K, which is

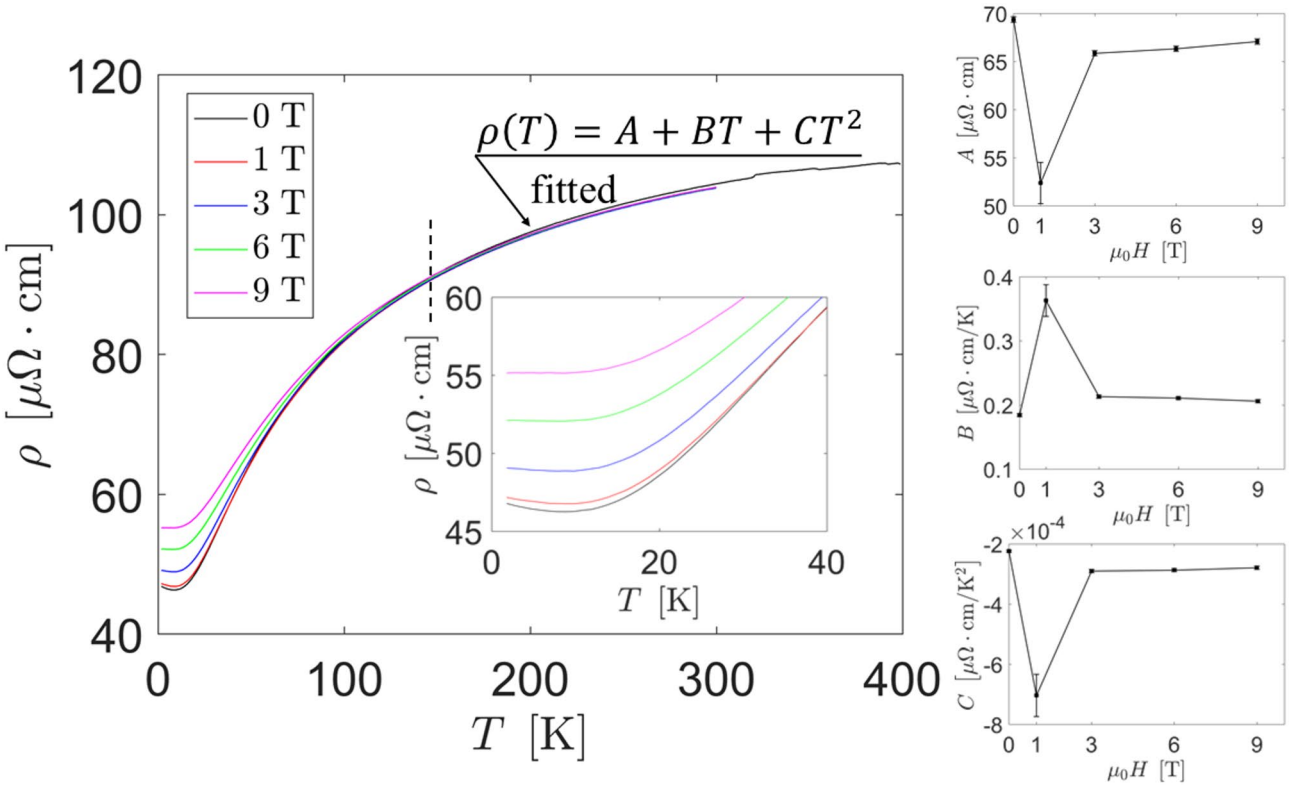

Fig. 17. The resistivity was measured at five magnetic field strengths. Above 150 K, the quadratic form of resistivity as a function of temperature was fitted. The parameters weakly depend on the magnetic field except for the measurement made at 1 T. However, the resistivity in this case was measured only up to 200 K, therefore, the fit does not capture the temperature dependence of the data well.

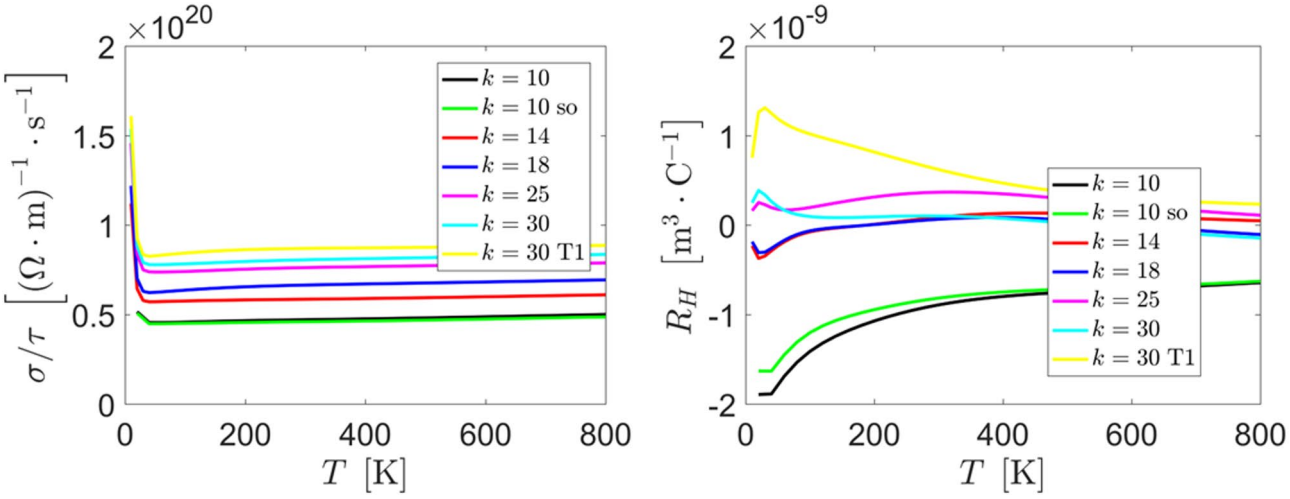

Fig. 18. Convergence of the electrical conductivity and Hall coefficient with respect to the k-mesh. Spin-orbit coupling was used for the B1 model with 10^3 mesh. The converged mesh 30^3 was used for further fitting for both T1 and B1.

a typical range for metals and semimetals[84]. The quadratic dependence of the resistivity is not the result of the temperature dependence of the carrier concentration but rather of the scattering mechanism.

The magnetoresistance was measured in the magnetic field up to 9 T. No sign of saturation is present, as shown in Fig. 20a. The shape of the magnetoresistance curve is linear. To confirm this, we fitted a power formula $\Delta\rho/\rho_0 = \alpha_{MR}(\mu_0 H)^{\delta} + c$. The range of the magnetic field was upper bound by four selected values. In all the cases, as shown in Fig. 20c, the exponent is subquadratic, ranging from 1.07 to 1.23 at 10 K. Semiclassical

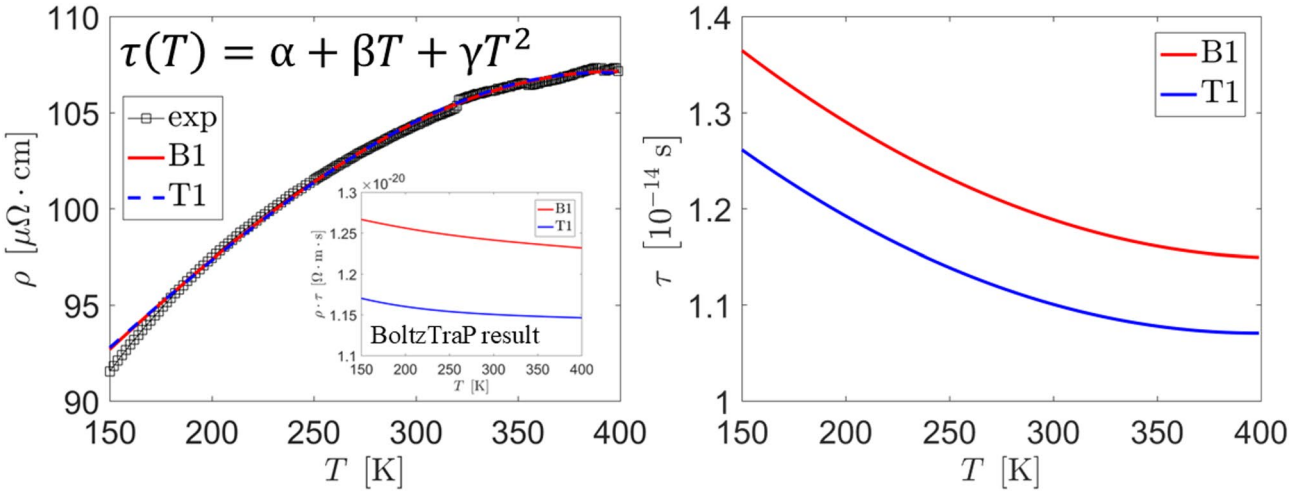

Fig. 19. (left) The fitted relaxation time formula based on theoretical data obtained from BoltzTraP and experimental data measured without a magnetic field. (right) Relaxation time as a function of temperature.

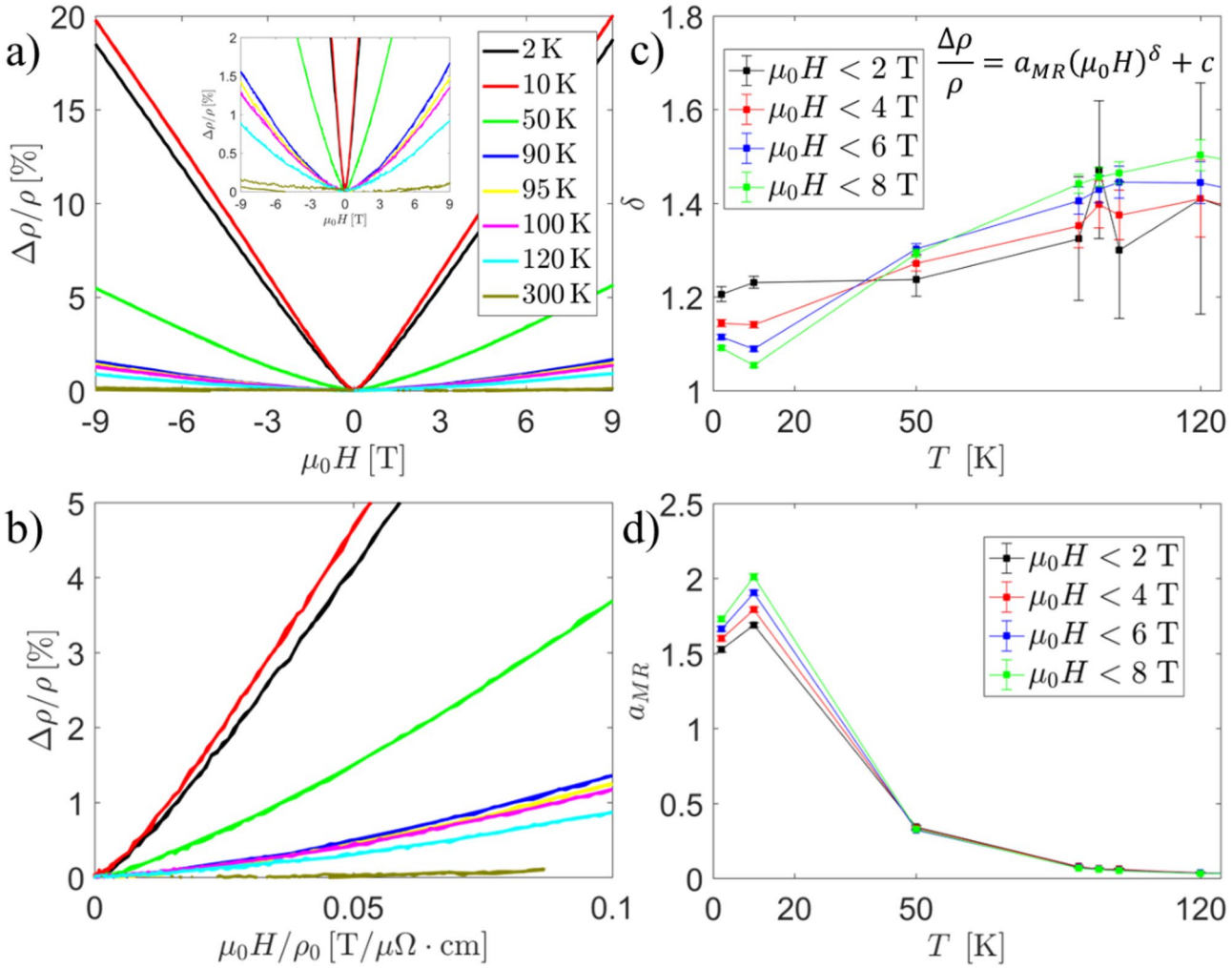

Fig. 20. (**a**) The magnetoresistance for selected temperatures. The fitted power law dependence of the magnetoresistance shows subquadratic behavior. The fit parameters are presented in (**c**,**d**). The fit is performed in regions where the magnetic field is upper-bound limited. In (**b**), the Kohler plot is shown, confirming the nonuniform scattering mechanism, as the curves are not superimposed.

theory of magnetoresistance predicts that when all the electron orbits are closed, the magnetoresistance increases in the form of $(\mu_0 H)^2$[85]. Linear magnetoresistance is observed in many charge density wave systems. On the basis of the model by Sinchenko et al.[86], linear magnetoresistance arises because of electron scattering on so-called "hot spots" of the Fermi surface, where the Fermi surface reconstruction due to the charge density wave is the strongest. The number of scattering "hot spots" in a quasicrystal is substantial because the periodic symmetry is broken. The effect is pronounced at low temperatures where electron–phonon scattering is low, as observed in our case. The temperature dependence of α_{MR} has a local peak at 10 K (Fig. 20d), which corresponds to the highest value of magnetoresistance. The peaks correlate with the lowest resistivity value observed in the resistivity data. Second, the highest value of the Hall coefficient calculated on the basis of B1 and T1 occurs above 0 K. In the classical theory of magnetoresistance, α_{MR} is proportional to the mobility of carriers. The mobility of carriers can be expressed as $\mu = |R_H|/\rho$, therefore, the lowest resistivity and the highest Hall coefficient result in a peak of α_{MR}. In Fig. 20b, deviation from Kohler scaling is observed[87]. In no region do the curves overlap, indicating nonuniform scattering mechanisms and the presence of multiple types of carriers. The nonuniform scattering mechanism helps explain the linear magnetoresistance due to the complexity of electron dispersion.

Summary

The electronic structure of the 1/1 periodic approximant crystal in the Zn-Mg-Hf Bergman-type system with $Pm\bar{3}$ was analyzed in detail via DFT methods. Two models were considered: B1, with an empty site corresponding to the position above the edge of the icosahedral shell, Zn14, and T1, where the site is fully occupied. Models are designed to mimic ideal Tsai and Bergman clusters. The center of the disordered body-centered cluster is filled with a fully occupied dodecahedral shell.

The T1 model was shown to be more stable with a scalar-relativistic approach, and the energy difference was calculated to be 10.9 meV per unit cell. This small energy difference justifies the observation that the atomic structure is positionally disordered, with fractional occupancies being balanced between those two models. The atomic structure of the approximant was shown to be stable at 0 K, but spin–orbit coupling must have been included in the calculations.

The introduction of atoms in Zn14 stie changes the local character of the orbitals, promoting the formation of bonding σ orbitals between Zn8 and Zn14. The interaction between Zn15 atoms changes to form a p-state peak at the Fermi level. The impact of atom introduction is marginal for atoms not in direct contact with Zn14. On the basis of the LDOS of Hf, the introduction of Zn14 makes the pseudogap narrower where the right edge of the pseudogap connects with the local peak at the Fermi level.

On the basis of partial charge population analysis via the Bader and Löwdin formalism, substantial charge transfer occurs between electronegative Zn and electropositive Mg and Hf atoms. The calculated Madelung energy follows the trend of formation enthalpy, indicating that the T1 model is more stable. This observation signifies the role of Coulomb interactions in the stabilization of the phase. The highest charge transfer between models occurs for atoms in a direct neighborhood to Zn14, i.e., Zn8 and Zn15. The higher positional stability of the vertex-centered cluster is also linked with increased charge transfer.

As indicated by reduced density gradient analysis, the introduction of atoms to the centers of clusters and the Zn14 site without changing the structure is not feasible because of steric conditions. The electron localization function indicates the presence of three-center and tetrahedral basins. The presence of three-enter and tetrahedral bonds is confirmed by Maximally Localized Wannier Function analysis. Three-center bonds are particularly formed in the vicinity of the Zn14 atom. Multicenter bonds are also predominant in the vertex-centered Bergman cluster, signifying the more pronounced stability of this configuration. The SCDM-k method was proven to work well in the complex structure of the periodic approximant of the quasicrystal.

Fermi surface analysis indicated the presence of nesting. The direction of the nesting vector is different for both models. Nesting occurs between surfaces with the highest electron velocity, resulting in both stable and conductive properties. Even though bare nesting is not enough for charge density formation, it might play a role in the formation of quasicrystals by considering strong electron–phonon coupling and the existence of phasons. Further studies might focus on the role of various factors in electronic structure modification. The pure Mott–Jones type of stabilization based on the Fermi-surface and Brillouin-zone interactions is unsatisfactory. Even though quasicrystals were found to obey the Hume–Rothery rule, the width and depth of the pseudogap significantly vary between phases. Additionally, hybridization cannot be the sole solution, as this is a local effect. The role of Fermi surface nesting and electron–phonon coupling, especially considering phonon–phason coupling, is an interesting direction of research toward revealing the stabilization mechanism of quasicrystals.

Electronic transport measurements performed on icosahedral F-type Zn-Mg-Hf ceramics revealed metallic resistivity behavior, with a minimum resistivity at approximately 10 K for measurements in a zero magnetic field. The high-temperature resistivity dependence is nonlinear, indicating complex scattering mechanisms. Theoretical calculations with Boltzmann transport in the relaxation time approximation confirm that the relaxation time has both linear and quadratic components. The magnetoresistance is subquadratic (almost linear) as a function of the magnetic field. No saturation is perceived. The best explanation is provided by the scattering of electrons on local bifurcations of the Fermi surface introduced by the nonperiodic potential. A similar model was proposed for charge density wave systems where linear magnetoresistance is frequently observed. The nontrivial scattering mechanism is confirmed but is a violation of Kohler scaling. Unlike other quasicrystals such as Al–Cu–Fe, quantum interference effects such as weak-localization and electron–electron interactions cannot be used to explain this phenomenon, as the magnitude of those effects is marginal compared with the observations. The fact that the resistivity of Zn-Mg-Hf is even two hundred times lower than that of Al-based quasicrystals is crucial.

The present conductive properties of quasicrystals have not been compared with those of the periodic approximant phase. It would be interesting to observe whether a nonlinear relaxation time and linear magnetoresistance are confirmed for the periodic phase.

Data availability

Data available upon request. Please contact Ireneusz Buganski (ireneusz.buganski@fis.agh.edu.pl).

Received: 29 May 2025; Accepted: 28 July 2025
Published online: 05 August 2025

References

1. Elser, V. & Henley, C. L. Crystal and quasicrystal structures in Al-Mn-Si alloys. *Phys. Rev. Lett.* **55**, 2883–2886 (1985).
2. Fujita, N., Takano, H., Yamamoto, A. & Tsai, A-P. Cluster-packing geometry for Al-based F-type icosahedral alloys. *Acta Cryst A*. **69**, 322–340 (2013).
3. Yamada, T., Takakura, H. & Yamamoto, A. Structure of face-centred icosahedral quasicrystal with cluster close packing. *Acta Cryst. A*. **80**, 422–438 (2024).
4. Ishimasa, T., Kaneka, Y. & Kaneko, H. A. Zn-based icosahedral quasicrystal classified into the same structure type as Cd-based icosahedral quasicrystals. *J. Alloys Comp.* **342**, 13–17 (2002).
5. Hasegawa, J., Takeuchi, S. & Tsai, A. P. Stable quasicrystals and approximants in Zn-Mg-Zr and Zn-Mg-Hf alloys. *Phil Mag Lett.* **85**, 289–297 (2005).
6. Buganski, I. et al. The structure solution of the F-type i-ZnMgHf from the X-ray diffraction. *Mat. Sci. Tech.* **36**, 989–995 (2020).
7. Ohhashi, S., Abe, E., Tanaka, M. & Tsai, A. P. Phase formation and structures of quasicrystals in Tge Zn-Mg-(Ti, zr, Hf) system. *Acta Mater.* **57**, 4727–4735 (2009).
8. Takakura, H., Gómez, C. P., Yamamoto, A., de Boissieu, M. & Tsai, A. P. Atomic structure of the binary icosahedral Yb-Cd quasicrystal. *Nat. Mat.* **6**, 58–63 (2007).
9. Li, M. R., Hovmöller, S., Sun, J. L., Zou, X. D. & Kuo, K. H. Crystal structure of the 2/1 cubic approximant $Ag_{42}In_{42}Yb_{16}$. *J. Alloys Compd.* **465**, 132–138 (2008).
10. Buganski, I. & Wolny, J. The equivalence of Tsai and Bergman clusters in 1/1 and 2/1 periodic approximant crystals. *J. Alloys Compd.* **939**, 168823 (2023).
11. Buganski, I., Strzalka, R. & Wolny, J. The physical space model of the Tsai-type quasicrystal. *Acta Cryst. B*. **80**, 84–93 (2024).
12. Gómez, C. P., Ohhashi, S., Yamamoto, A. & Tsai, A. P. Disordered structures of the TM-Mg-Zn 1/1 quasicrystal approxiamnts (TM = Hf, Zr or Ti) and chemical intergrowth. *Inorg. Chem.* **47**, 8258–8266 (2008).
13. Buganski, I., Strzalka, R. & Wolny, J. The Tsai vs Bergman cluster stability in ZnMgSc 1/1 periodic approximant crystal. *Isr. J. Chem.* **64**, e202300139 (2024).
14. Giannozzi, P. et al. QUANTUM ESPRESSO: a modular and open-source software project for quantum simulations of materials. *J. Phys. : Condens. Matter*. **21**, 395502 (2009).
15. Giannozzi, P. et al. Advanced capabilities for materials modelling with QUANTUM ESPRESSO. *J. Phys. : Condens. Matter*. **29**, 465901 (2017).
16. Giannozzi, P. et al. QUANTUM ESPRESSO toward the exascale. *J. Chem. Phys.* **152**, 154105 (2020).
17. Takeda, T. The scalar relativistic approximation. *Z. Phys. B*. **31**, 43–48 (1978).
18. Pedrew, J., Burke, K. & Ernzerhof, M. Generalized gradient appxoximation made simple. *Phys. Rev. Lett*. **77**, 386 (1996).
19. Monkhorst, H. J. & Pack, J. D. Special points for Brillouin-Zone integrations. *Phys. Rev. B*. **13**, 5188–5192 (1976).
20. dos Santos, F. J. & Marzari, N. Fermi energy determination for advanced smearing techniques. *Phys. Rev. B*. **107**, 195122 (2023).
21. Methfessel, M. & Paxton, A. T. High-precision sampling for Brillouin-zone integration in metals. *Phys. Rev. B*. **40**, 3616 (1989).
22. Pizzi, G. et al. Wannier90 as a community code: new features and applications. *J. Phys. : Cond Matt*. **32**, 165902 (2020).
23. Damale, A., Lin, L. & Ying, L. SCDM-k: localized orbitals for solids via selected columns of the density matrix. *J. Comp. Phys.* **334**, 1–15 (2017).
24. Dudarev, S. L., Botton, G. A., Savrasov, S. Y., Humphreys, C. J. & Sutton, S. P. Electron-energy-loss spectra and the structural stability of nickel oxide: an LSDA + U study. *Phys. Rev. B*. **57**, 1505 (1998).
25. Madsen, G. K. H. & Singh, D. J. BoltzTraP. A code for calculating band-structure dependent quantities. *Comp. Phys. Comm.* **175**, 67–71 (2006).
26. Yu, Y., Fang, D., Zhao, G. D. & Zheng, X. L. *Ab initio* calculations of the thermodynamic properties of wurtzite zns: performance of the LDA and GGA. *Chalcog Lett.* **11**, 619–628 (2014).
27. Jana, S., Sharma, K. & Samal, P. Assessing the performance of the recent meta-GGA density functionals for describing the lattice constants, bulk moduli, and cohesive energies of alkali, alkaline-earth, and transition metals. *J. Chem. Phys.* **149**, 164703 (2018).
28. Samson, S. Die Kristallstruktur des Mg2Zn11. Isomorphie Zwischen Mg2Zn11 und Mg2Cu6Al5. *Acta Chem. Scand.* **3**, 835–843 (1949).
29. Green, S. P., Jones, C. & Stasch, A. Stable Magnesium(I) compounds with Mg-Mg bonds. *Science* **318**, 1754–1757 (2007).
30. de Boissieu, M. Phonons, phasons and atomic dynamics in quasicrystals. *Chem. Soc. Rev.* **41**, 6778–6786 (2012).
31. de Boissieu, M. et al. Lattice dynamics of the Zn-Mg-Sc icosahedral quasicrystal and its Zn-Sc periodic 1/1 approximant. *Nat. Mat.* **6**, 977–984 (2007).
32. Tamura, R. et al. Universal low-temperature phase transition in Zn- and Cd-based crystalline approximants. *Phys. Rev. B*. **71**, 092203 (2005).
33. Widom, M. Discussion of phasons in quasicrystals and their dynamics. *Phil Mag*. **88**, 2339–2350 (2008).
34. Ishii, Y. & Fujiwara, T. Hybridization mechanism for cohesion of Cd-Based quasicrystals. *Phys. Rev. Lett.* **87**, 206408 (2001).
35. Mizutani, U., Takeuchi, T. & Sato, H. Interpretation of the Hume-Rothery rule in quasicrystals and their approximants. *J. Non-Cryst Sol*. **334&335**, 331–335 (2004).
36. Mizutani, U., Takeuchi, T. & Sato, H. Interpretation of the Hume-Rothery rule in complex electron compounds: γ -Cu_5Zn_8 Alloy, FK = type $Al_{30}Mg_{40}Zn_{30}$ and MI-type $Al_{68}Cu_7Ru_{17}Si_8$ 1/1–1/1–1/1 approximants. *Prog Mat. Sci.* **49**, 227–261 (2004).
37. Tamura, R. et al. Experimental evidence for *p-d* hybridization in the Cd-Ca quasicrystal: origin of the pseudogap. *Phys. Rev. Lett.* **92**, 146402 (2004).
38. Freitag, K. et al. Zn-Zn interactions at nickel and palladium centers. *Royal Soc. Chem.* **7**, 6413–6421 (2016).
39. Löwdin, P. O. On the Non-Orthogonality problem connected with the use of atomic wave functions in the theory of molecules and crystals. *J. Chem. Phys.* **18**, 365–375 (1950).
40. Mulliken, R. S. Electronic population analysis on LCAO-MO molecular wave functions. *I J. Chem. Phys.* **23**, 1833–1840 (1955).
41. Bader, R. F. A quantum theory of molecular structure and its applications. *Chem. Rev.* **91**, 893–928 (1991).
42. Henkelman, G., Arnaldsson, A. & Jonsson, H. A. Fast and robust algorithm for bader decomposition of charge density. *Comp. Mat. Sci.* **36**, 354–360 (2006).

43. Tang, W., Sanville, E. & Henkelman, G. A grid-based bader analysis algorithm without lattice bias. *J. Phys. : Condens. Matter*. **21**, 084204 (2009).
44. Agnarelli, L. et al. $Mg_{29-x}Pt_{4+y}$: chemical bonding inhomogenity and structural complexity. *Inorg. Chem.* **61**, 16148–16155 (2022).
45. Amon, A. et al. Cluster formation in the superconducting complex intermetallic compound $Be_{21}Pt_5$. *Acc. Chem. Res.* **51**, 214–222 (2018).
46. Lee, C. S. & Miller, G. J. Experimental and theoretical studies of elemental site preferences in quasicrystalline approximants (R-Phases) within Li-Mg-Zn-Al system. *Inorg. Chem.* **40**, 338–345 (2001).
47. Buxi, K., Mondal, A., Wang, F. & Jana, P. P. Structural and theoretical investigations on the coloring scheme of γ-brass type phase Ag5Cd8. *J. Solid State Chem.* **323**, 124019 (2023).
48. Zintl, E., Intermetallishe & Verbindungen *Angew Chem.* **52**, 1–6 (1939).
49. Kauzlarich, S. M. Zintl phases: from curiosities to impactful materials. *Chem. Mat.* **35**, 7355–7362 (2023).
50. Mizutani, U. & Sato, H. The physics of the Hume-Rothery electron concentration rule. *Crystals* **7**, 1–112 (2017).
51. Kato, D. et al. Valance band engineering of layered bismuth oxyhalides toward stable Visible-Light water splitting: Madelung site potential analysis. *J. Am. Chem. Soc.* **129**, 18725–18731 (2017).
52. Pauling, L. The principles determining the structure of complex ionic crystals. *J. Am. Chem. Soc.* **51**, 1010–1026 (1929).
53. Ertural, C., Steinberg, S. & Dronskowski, R. Development of a robust tool to extract mulliken and Löwdin charges from plane waves and its application to solid-state materials. *RSC Adv.* **9**, 29821 (2019).
54. Glasser, L. Solid-State energetics and electrostatics: Madelung constants and Madelung energies. *Inorg. Chem.* **51**, 2420–2424 (2012).
55. Momma, K. & Izumi, F. VESTA 3 for Three-Dimensional visualization of crystal, volumetric and morphology data. *J. App Cryst.* **44**, 1272–1276 (2011).
56. Wyckoff, R. W. G.*Crystal Structures* Second Edition 7–83 (Interscience Publisher, 1963).
57. Becke, A. D. & Edgecombe, K. E. A simple measure of electron localization in atomic and molecular systems. *J. Chem. Phys.* **92**, 5397–5403 (1990).
58. Silvi, B. & Savin, A. Classification of chemical bonds based on topological analysis of electron localization functions. *Nature* **371**, 683–686 (1994).
59. Silvi, B. & Gatti, C. Direct representation of the metallic bond. *J. Phys. Chem. A*. **104**, 947–953 (2000).
60. Conteras-Garcia, J., Pendas, A. M., Silvi, B. & Recio, J. M. Useful applications of the electron localization function in high-pressure crystal chemistry. *J. Phys. Chem. Sol*. **69**, 2204–2207 (2008).
61. Sun, Y. et al. Chemical interactions that govern the structures of metals. *PNAS* **120**, e2218405120 (2023).
62. Silvi, B. The synaptic order: a key concept to understand multicenter bonding. *J. Mol. Str.* **614**, 3–10 (2002).
63. Johnson, E. R. et al. Revelaing noncovalent interactions. *J. Am. Chem. Soc.* **132**, 6498–6506 (2010).
64. Marzari, N., Mostofi, A. A., Yates, J. R., Souza, I. & Vanderbilt, D. Maximally localized Wannier functions: theory and applications. *Rev. Mod. Phys.* **84**, 1419 (2012).
65. Kitahara, K., Takagiwa, Y. & Kimura, K. Semimetallic band structure and Cluster-Based description of a cubic quasicrystalline approximant in the Al-Cu-Ir system. *J. Phys. Soc. Jpn*. **84**, 014703 (2015).
66. Kitahara, K. & Kimura, K. Local cluster networks and the number of Valance States in aluminium-transition metal face-centered icosahedral quasicrystals. *Z. Kristallogr. – Cryst. Mater.* **232**, 507–513 (2017).
67. Iwasaki, Y., Kimura, K. & Kitahara, K. Three-Center bonds in an Al-Pd-Co quasicrystalline approximant: Wannier function-Based chemical bonding analysis. *J. Phys. Chem. C*. **127**, 20945–20950 (2023).
68. Katz, A. & Gratias, D. A geometric approach to chemical ordering in icosahedral structures. *J. Non Cryst. Sol.* **153–154**, 187 (1993).
69. Cornier-Quiquandon, M. et al. Neutron-diffraction study of icosahedral Al-Cu-Fe single quasicrystals. *Phys. Rev. B*. **44**, 2071 (1991).
70. Boudard, M. et al. Neutron and X-ray single-crystal study of the AlPdMn icosahedral phase. *J. Phys. : Cond Matt*. **4**, 10149 (1992).
71. Vitale, V. et al. Automated high-throughput wannierisation. *Comput. Mat.* **6**, 66 (2020).
72. Kawakami, T. et al. Charge-density wave associated with higher-order Fermi-surface nesting in monolayer VS_2, *npj 2D Mater. Appl* **7**, 35 (2023).
73. Roche, S. & Fujiwara, T. Fermi surfaces and anomalous transport in quasicrystals. *Phys. Rev. B*. **58**, 11338 (1998).
74. Krajčí, M. & Hafner, J. Fermi surfaces and electronic transport properties of quasicrystalline approximants. *J. Phys. : Condens. Matter*. **13**, 3817–3830 (2001).
75. Kawamura, M. & FermiSurfer Fermi-surface viewer procviding multiple representation schemes. *Comp. Phys. Comm*. **239**, 197–203 (2019).
76. Johannes, M. D. & Mazin, I. I. Fermi surface nesting and the origin of charge density waves in metals. *Phys. Rev. B*. **77**, 165135 (2008).
77. Zhu, X., Cao, Y., Zhang, J., Plummer, E. W. & Guo, J. Classification of charge density wave based on their nature. *Proc. Natl. Acad. Sci.* **112**, 2367–2371 (2015).
78. Shuyuan, L., Guohong, L. & Dianlin, Z. Thermopower of Decagonal $Al_{73}Ni_{17}Co_{10}$ Single Quasicrystals: Evidence for a Strongly Enhanced Electron-Phonon Coupling in the Quasicrystalline Plane. *Phys. Rev. Lett.***77**, 1998 (1996).
79. Ahlgren, M., Rodmar, M., Sommer, M. & Rapp, Ö. Vanishing Coulomb interaction parameter F_σ with increasing temperature in AlCuFe-quasicrystal. *J. Non Cryst. Sol*. **205–207**, 21–24 (1996).
80. Aoyama, M., Ohhashi, S., Takakura, H., Iwasaki, Y. & Fujita, N. Highly tunable icosahedral orders in complex Al-Pd-W-Fe alloys. *J. Alloys Compd.* **1016**, 178838 (2025).
81. Pope, A. L., Tritt, T. M., Gagnon, R. & Strom-Olsen, J. Electronic transport in Cd-Yb and Y-Mg-Zn quasicrystals. *App Phys. Lett.* **79**, 2345 (2001).
82. Giannò, K. et al. Electrical resistivity, thermopower, and thermal conductivity of single grained (Y, tb, ho, Er)-Mg-Zn icosahedral quasicrystals. *Mat. Sci. Eng.* **294–296**, 715–718 (2000).
83. Mihalkovič, M. & Widom, M. F. Enthalpies of Al-Mn-Pd and the structure of the i-AlMnPd quasicrystal. *Rend. Lincei Sci. Fis. Nat.* **34**, 671–680 (2023).
84. Singh, S., Kumar, D. & Pandey, K. Experimental and theoretical investigations of thermoelectric properties of $La_{0.82}Ba_{0.18}CoC_3$ compound in high temperature region. *Phys. Lett. A*. **381**, 3101–3106 (2017).
85. Diaz, J. et al. Semi-classical origin of the extreme magnetoresistance in $PtSn_4$. *Nat. Comm.* **15**, 4585 (2024).
86. Sinchenko, A. A., Grigoriev, P. D., Lejay, P. & Monceau, P. Linear magnetoresistance in the charge density wave state of quasi-two-dimensional rare-earth tritellurides. *Phys. Reb B*. **96**, 245129 (2017).
87. Kohler, M. Zur Magnetischen widerstandsänderung Reiner Metalle. *Ann. Phys.* **424**, 211 (1938).

Acknowledgements

I. B., R. S. and J. W. acknowledge financial support from the National Science Center of Poland under grant no. 2022/47/I/ST3/00340. S. V and J. L. acknowledge the financial support from the Slovenian Research and Innovation Agency (Research Core Funding No. P1-0125 and Project No. N1-0330). We gratefully acknowledge the Polish high-performance computing infrastructure PLGrid (HPC Centers: ACK Cyfronet AGH) for provid-

ing computer facilities and support within computational grant no. PLG/2024/017147. Open access publication was supported by the AGH University of Krakow under programme IDUB "Excellence Initiative – Research University". All figures were generated by the authors. Programs used for figures: Microsoft Office 16 PowerPoint (URL: https://www.office.com/), Blender v. 4.1 (URL: https://www.blender.org/), MATLAB R2024a (URL: https://www.mathworks.com/products/matlab.html), FermiSurfer 2.4.0 (URL: https://mitsuaki1987.github.io/fermisurfer/). The software used for calculations: BoltzTraP v.1.2.5 (URL: https://www.tuwien.at/en/tch/tc/theoretical-materials-chemistry/boltztrap), QUANTUM ESPRESSO v.6.7 (URL: https://www.quantum-espresso.org/), Wannier90 v.2.1.0 (URL: https://wannier.org/), VESTA v.4.6.0 (URL: https://jp-minerals.org/vesta/en/).

Author contributions

I. B. conceived the study, performed electronic structure calculations and data interpretation, including DFT and electronic transport analysis; secured the funding and access to computational cluster; contributed to the manuscript and figure preparation. S. V. performed electronic transport and magnetization measurements and contributed to transport data analysis. R.S. contributed to data analysis and revision of the manuscript. J. L. performed electronic transport and magnetization measurements. J.W. contributed to atomic structure verification regarding the used model and manuscript revision. N. F. provided the facility to prepare the sample and contributed to data analysis and manuscript revision.

Declarations

Competing interests

The authors declare no competing interests.

Additional information

Supplementary Information The online version contains supplementary material available at https://doi.org/10.1038/s41598-025-13835-1.

Correspondence and requests for materials should be addressed to I.B.

Reprints and permissions information is available at www.nature.com/reprints.

Publisher's note Springer Nature remains neutral with regard to jurisdictional claims in published maps and institutional affiliations.